The Hydrologic and Thermodynamic Characteristics of the NCAR CCM3*

James J. Hack, Jeffrey T. Kiehl, and James W. Hurrell

National Center for Atmospheric Research,+ Boulder, Colorado

(Manuscript received 15 May 1997, in final form 29 September 1997)

ABSTRACT

Climatological properties for selected aspects of the thermodynamic structure and hydrologic cycle are presented from a 15-yr numerical simulation conducted with the National Center for Atmospheric Research Community Climate Model, version 3 (CCM3), using an observed sea surface temperature climatology. In most regards, the simulated thermal structure and hydrologic cycle represent a marked improvement when compared with earlier versions of the CCM. Three major modifications to parameterized physics are primarily responsible for the more notable improvements in the simulation: modifications to the diagnosis of cloud optical properties, modifications to the diagnosis of boundary layer processes, and the incorporation of a penetrative formulation for deep cumulus convection. The various roles of these physical parameterization changes will be discussed in the context of the simulation strengths and weaknesses.

1. Introduction

One of the more important long-standing problems in global modeling of the climate system and its sensitivity to increased greenhouse gases is how to accurately include the effects of the various components of the hydrologic cycle into the governing meteorological equations. In the past, earth's hydrologic cycle has been characterized as an aspect of the climate system that was simply controlled by the general circulation (e.g., see Riehl 1965). It is now clear, however, that the details of evaporation, precipitation, runoff, and water transport are very much an integral part of the general circulation, representing a major component of the overall energy budget, particularly for the thermally driven circulations in the Tropics and subtropics (Chahine 1992).

Water in any phase is a strongly radiatively active atmospheric constituent, and changes in water phase are a major source of diabatic heating in the atmosphere. Consequently, the large-scale moisture field plays a fundamental role in the maintenance of the general circulation and climate, where the sources, sinks, and a large component of the transport responsible for its time evolution are inadequately understood. It is generally recognized that our ability to numerically model climate and climate change is fundamentally limited by a lack of understanding of the interaction of moist processes and the large-scale radiation field, particularly with respect to clouds (e.g., Stephens and Webster 1981; Cess et al. 1990). Clouds are a central component in the hydrologic cycle since they directly couple dynamical and hydrological processes in the atmosphere through the release of the latent heat of condensation and evaporation, through precipitation, and through the vertical redistribution of sensible heat, moisture, and momentum. They play an equally critical role in the large-scale thermodynamic budget through the reflection, absorption, and emission of radiation, and they are directly involved in the chemistry of the earth's atmosphere. Efforts to realistically incorporate these processes on a planetary scale are hampered by the wide range of important space and time scales contained in the atmosphere's general circulation. Cloud-scale processes involving phase change influence the behavior of the atmosphere on all time and space scales but operate on scales of motion distinctly separate from those of the larger-scale circulation. Because of this scale separation, their collective effects on the general circulation are parameterized as a function of the large-scale fields. The form of the parameterized treatment of the principal components of the hydrologic cycle strongly influences the fidelity of global climate simulations.

The formulation of the National Center for Atmospheric Research (NCAR) Community Climate Model version 2 (CCM2) was a significant departure from earlier versions of the CCM, which suffered from highly simplified physical parameterizations, particularly for the determination of surface temperature, surface energy exchanges, boundary layer transfers, moist convection,

and the diagnosis of cloud amount and its interaction with the radiation field. Most of the CCM1 physical parameterization components were replaced with considerably more sophisticated methods for treating these key climate processes (Hack et al. 1993). Although many aspects of the CCM2 simulation have been shown to be significantly more realistic when compared with predecessor models (e.g., Hack et al. 1994; Kiehl et al. 1994; Hurrell et al. 1993), a number of important systematic deficiencies continued to plague the simulation, many of which would introduce serious climate drifts if the CCM2 were to be coupled to interactive land, sea-ice, and ocean component models. One of the more glaring weaknesses included several aspects of the simulated hydrologic cycle, which was extremely active when compared to observational estimates (e.g., Lau et al. 1995).

A principal objective for the development of the CCM3 was to address the more serious systematic errors present in the CCM2 simulation, so as to make the atmospheric model more suitable for coupling to other climate component models, such as in the NCAR Climate System Model described by Boville and Gent (1998). The vast majority of this development activity therefore focused on further improving the formulation of several key physical parameterizations (Kiehl et al. 1996). These improvements are reflected in a considerably more credible climate simulation for the CCM3 (e.g., Kiehl et al. 1998a; Kiehl et al. 1998b; Hurrell et al. 1998). In this paper we will discuss selected aspects of the thermodynamic structure and hydrologic cycle as simulated by CCM3. We will examine characteristics of the mean state, annual cycle, and aspects of variability in response to El Niño–Southern Oscillation (ENSO). We will also discuss the physical reasons for these characteristics in the context of the changes in physical parameterization. Comparisons will be made with available observational data. Since there is considerable uncertainty in many measures of the hydrological cycle, and some aspects are not observed on a global basis, we will also occasionally include CCM2 simulation results to provide a stable reference point for illustrating how selected simulation metrics have changed.

2. Parameterization changes and the global hydrologic cycle

The CCM3 is the fourth generation in the series of NCAR's Community Climate Model. Most aspects of the model's dynamical formulation and implementation are identical to the CCM2. The most important changes to the model formulation have been made to the collection of parameterized physics. When compared to the CCM2, changes to the physics most relevant to the global hydrological cycle fall into three major categories: modifications to the representation of radiative transfer through both clear and cloudy atmospheric columns; modifications to the atmospheric boundary layer, moist convection, and surface energy exchange formulations; and the incorporation of a sophisticated and comprehensive land surface model (LSM) developed by Bonan (1996). The LSM is a one-dimensional model of energy, momentum, water, and CO_2 exchange between the atmosphere and land. It accounts for ecological differences among vegetation types, hydraulic and thermal differences among soil types, and allows multiple surface types, including lakes and wetlands, within a single grid cell. LSM replaces the prescribed surface wetness, prescribed snow cover, and prescribed surface albedos employed in the CCM2, as well as the CCM2 mathematical formulations for evaluating land surface fluxes. The incorporation of the land surface model greatly improves regional aspects of the simulated surface climate, particularly with regard to diurnal and seasonal cycles, where the specific simulation characteristics are shown in Bonan (1998) and will not be examined here.

Let us begin by discussing the remaining two categories of modified physics components in the context of globally and annually averaged properties of the CCM3 simulated climate, the CCM2 simulated climate, and the corresponding observational estimates (shown in Table 1). These particular global averages are highly stable measures of model performance, where even relatively small differences generally indicate significant systematic changes in the simulation properties. We begin with the suite of changes incorporated in the parameterization of clouds and radiation. Changes to the clear-sky radiation formalism include the incorporation of trace gases (CH_4, N_2O, CFC11, CFC12) and some minor CO_2 bands in the longwave parameterization, and the incorporation of a background aerosol in the shortwave parameterization (Kiehl et al. 1998a). All-sky changes include improvements to the way in which cloud optical properties are diagnosed (Kiehl 1994a; Hack 1998a), the incorporation of the radiative properties of ice clouds, and several other minor modifications to the parameterization of convective and layered cloud amount (Kiehl et al. 1998a). The global impact of these modifications can be seen in Table 1, where systematic biases in the clear-sky and all-sky outgoing longwave radiation and absorbed solar radiation are substantially reduced to well within observational uncertainty, while maintaining very good agreement with global observational estimates of cloud forcing. The principal effect of the clouds and radiation modifications is to improve the top-of-atmosphere (TOA) and surface energy budgets, both regionally and globally (e.g., see Kiehl et al. 1998b). In particular, these parameterization changes greatly reduce net surface solar radiation resulting in a decrease in the warm July surface temperature bias over the Northern Hemisphere, reductions in the systematic overprediction of precipitation over warm land areas, and improvements in the simulated stationary wave structure (e.g., see Hack 1998a). The reduction in the global annual latent heat flux (which we will use as one measure of the overall strength of

TABLE 1. Global annual average properties.

	Observations	CCM2	CCM3
Outgoing longwave radiation (W m^{-2})			
all sky	234.8[a]	241.10	236.97
clear sky	264.0[a]	271.87	266.22
Absorbed solar radiation (W m^{-2})			
all sky	238.1[a]	245.35	236.88
clear sky	286.3[a]	295.49	286.42
Longwave cloud forcing (W m^{-2})	29.2[a]	30.76	29.25
Shortwave cloud forcing (W m^{-2})	-48.2[a]	-50.14	-49.54
Cloud fraction (percent)			
total	52.2[b]–62.5[c]	52.86	58.83
low	26.0[c]–43.8[d]	30.52	34.75
middle	18.0[c]	22.20	20.84
high	14.0[c]	28.89	34.62
Cloud water path (mm)	0.0700–0.0813[e]	—	0.0465
Precipitable water (mm)	24.7[f]	25.52	23.39
Latent heat flux (W m^{-2})	78.0[h]	104.04	89.97
Sensible heat flux (W m^{-2})	24.0[h]	9.32	20.47
Precipitation (mm day^{-1})	2.69[g]	3.58	3.09
Net surface solar radiation (W m^{-2})	168[h]	180.89	171.05
Net surface longwave radiation (W m^{-2})	66[h]	62.58	60.68
Annual mean budgets (W m^{-2})			
TOA energy budget		4.25	-0.09
surface energy budget		4.95	-0.07
total water ($P - E$)		0.00	0.00

[a] ERBE.
[b] *Nimbus-7* (Hurrell and Campbell 1992).
[c] ISCCP (Rossow and Zhang 1995).
[d] Warren et al. (1988).
[e] Greenwald et al. (1995), all-sky average.
[f] NVAP (Randel et al. 1996).
[g] Xie and Arkin (1996).
[h] Kiehl and Trenberth (1997).

the hydrologic cycle) associated with cloud optical property changes represents approximately 3 W m^{-2} of the decrease shown between CCM2 and CCM3.

The remaining category of physics changes have the greatest impact on the simulated hydrologic cycle. The first of these includes revisions to the formulation of the atmospheric boundary layer (ABL) parameterization, resulting in greatly improved estimates of boundary layer height, and a substantial reduction in the overall magnitude of the hydrologic cycle, approximately 8 W m^{-2} in the global annual mean when compared to the CCM2. Since the ABL modifications minimally affect the net surface energy balance, the reduction in latent heat flux is offset by a comparable increase in sensible heat flux (as seen in Table 1). Thus, the revised boundary layer formulation results in a more realistic partitioning of the surface turbulent heat flux. Parameterized convection has also been modified in CCM3 where moist convection is now represented using the deep cumulus formalism of Zhang and McFarlane (1995) in conjunction with the scheme developed by Hack (1994) for the CCM2. A Sundqvist (1988) style evaporation of stratiform precipitation is also incorporated in the CCM3, playing an important role in maintaining the simulated

thermodynamic structure of the lower troposphere. These changes result in an additional reduction to the magnitude of the global hydrologic cycle (approximately 3 W m^{-2}) along with a number of other desirable improvements, such as a smoother distribution of tropical precipitation and a warmer tropical troposphere. The additional reduction in latent heat flux is generally confined to regions of deep convection, most notably in the ITCZ, and is the singlemost important simulation feature contributing to the improvement in the implied meridional ocean heat transport (Hack 1998b). Other noteworthy changes in global measures associated with the modified convection parameterization are a large increase in high cloud amount and a decrease in precipitable water (see Table 1). Finally, surface roughness over ocean surfaces is diagnosed as a function of surface wind speed and stability in the CCM3, resulting in more realistic surface flux estimates for low wind speed conditions. The combination of these changes to the major moist physics parameterizations results in more than a 10% reduction in the annually averaged global latent heat flux and the associated precipitation rate.

Several of the more relevant global measures of the hydrologic cycle exhibit interesting, albeit relatively

Annual Cycle of Precipitable Water

Annual cycle of precipitation
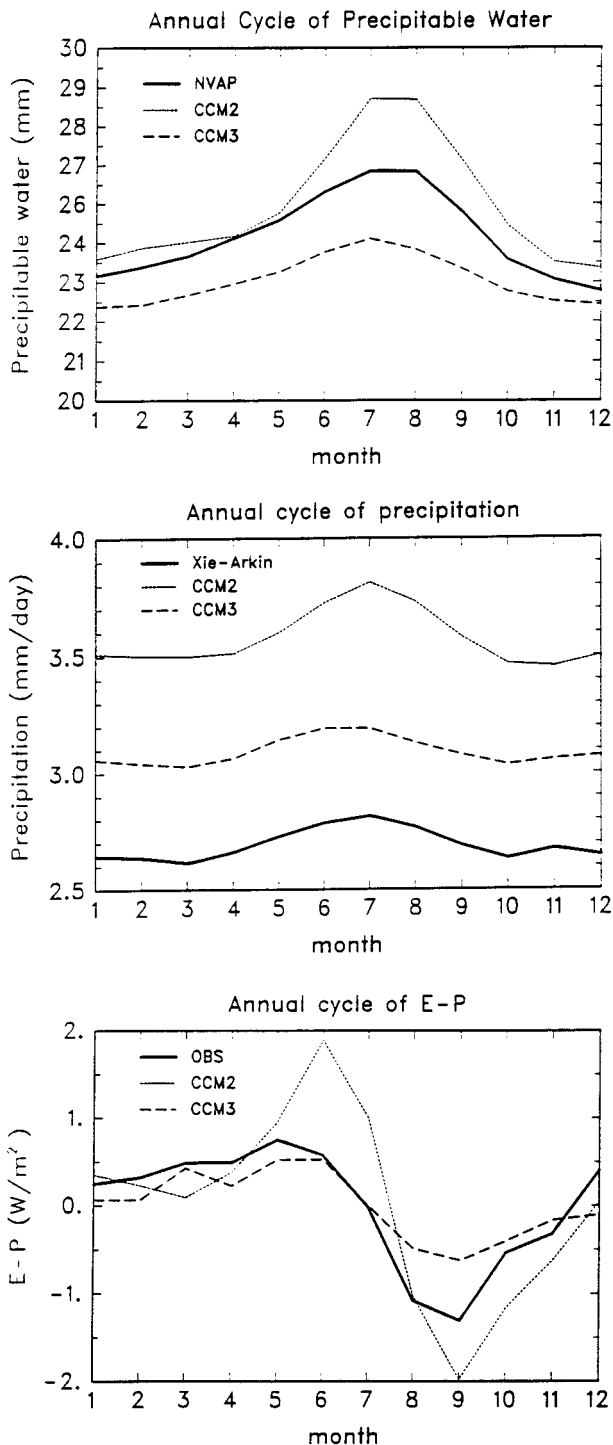

Annual cycle of E-P

FIG. 1. Annual cycle of globally averaged precipitable water, precipitation, and $E - P$, for the CCM3 and corresponding observational estimates.

weak, seasonal behaviors. Figure 1 shows the seasonal cycle of precipitable water (representing the storage of water vapor in the atmosphere), precipitation, and the difference between evaporation and precipitation, for

the CCM2, CCM3, and the corresponding observational estimates. The estimates of precipitation rate are taken from Xie and Arkin (1996), who have constructed global distributions of monthly precipitation by combining data from gauge observations, several different satellite retrieval estimates, and predictions from the European Centre for Medium-Range Weather Forecasts (ECMWF) operational forecast model. Observational estimates of precipitable water are taken from the National Aeronautics and Space Administration (NASA) Water Vapor Project (NVAP), which combines water vapor retrievals from the *TIROS-N* Operational Verticle Sounder (TOVS) and the Special Sensor Microwave/ Imager (SSM/I) platforms with radiosonde observations (Randel et al. 1996).

The CCM simulations and NVAP analysis all show a clear annual cycle in precipitable water, with minima in December and maxima during July and August. The CCM2 exhibits the largest global water vapor content and the largest amplitude in the global annual cycle, 4.9 mm compared with just under 3.5 mm shown in the NVAP data. The CCM3 is systematically drier than the NVAP estimates, approximately 1.3 mm in the global annual mean, with a slightly weaker annual amplitude of just under 2.0 mm. Kiehl et al. (1998a) attribute the remaining bias in the TOA clear-sky OLR to the precipitable water dry bias present in the CCM3 simulation. In all cases the global annual cycles shown in the first panel of Fig. 1 are dominated by a stronger seasonal cycle in precipitable water over the Northern Hemisphere. The seasonal cycle in precipitable water is fueled by an imbalance in the globally averaged evaporation and precipitation, where the precipitation term exhibits a similar seasonal peak during the Northern Hemisphere summer months. The imbalance responsible for the annual cycle in precipitable water turns out to be very small, measured in fractions of a watt per square meter, as shown in the third panel (where the curve labeled OBS is derived from the NVAP and Xie and Arkin datasets). As suggested by the first two panels, the CCM3 does a good job of simulating the phase of this imbalance with slightly weaker amplitude when compared to the observational estimates. The CCM2 shows noticeable differences in both amplitude and phase.

Another important role of water in the atmosphere is in the form of clouds. Although cloud condensate is not carried as a prognostic variable in the CCM3, it is a diagnosed quantity that strongly affects the global radiation budget. In the global annual mean the vertically integrated condensed water (or cloud water path) is considerably smaller than the atmospheric water vapor content, but contributes to an important radiative forcing on the climate system as measured by longwave and shortwave cloud forcing (see Table 1). The globally averaged cloud fraction exhibits a clear seasonal cycle in both the CCM2 and CCM3, with maximum cloud amount occurring during the Northern Hemisphere winter months (Fig. 2). A comparable seasonal cycle is not
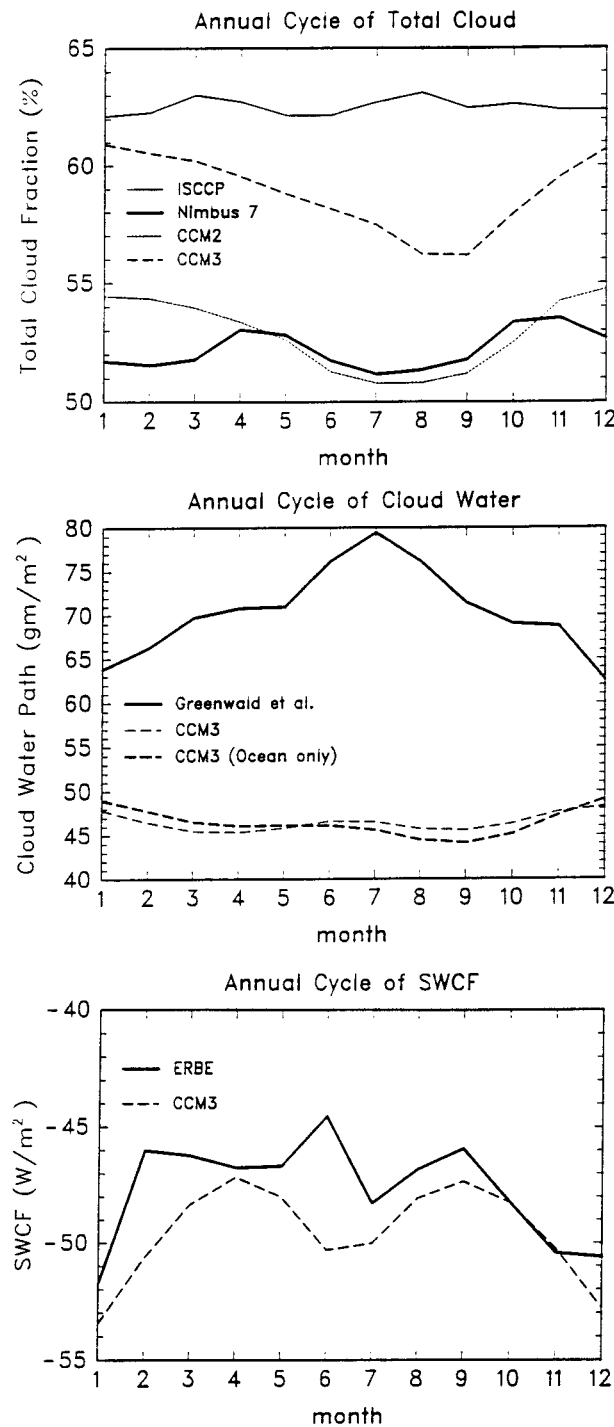
FIG. 2. Annual cycle of globally averaged total cloud, cloud water, and shortwave cloud forcing (SWCF), for the CCM3 and corresponding observational estimates.

seen in either of the corresponding observational datasets, which are derived from International Satellite Cloud Climatology Project (ISCCP) (Rossow and Zhang 1995) and from *Nimbus-7* (Hurrell and Campbell 1992). The ISCCP and *Nimbus-7* observations bracket the

CCM2 and CCM3 results, where the CCM3 cloud amount is systematically larger than in CCM2 throughout the entire year. The greater total cloud amount in CCM3 is largely the result of an increase in high cloud that accompanied the introduction of the Zhang–Mc-Farlane scheme for treating deep cumulus convection.

The CCM3 annual cycle in cloud amount is reflected in a somewhat similar seasonal variation in condensed water, as shown in the middle panel of Fig. 2, where the principal maximum in cloud water path occurs in January, with a weak secondary maximum occurring during June and July. The satellite-derived cloud liquid water path data obtained from Greenwald et al. (1995) shows a distinct seasonal cycle, but with a much stronger amplitude and virtually completely out of phase with the CCM3. The Greenwald et al. (1995) data are for the 4-yr period 1988–91, and represent an ocean-only *all-sky* field of view for nonprecipitating clouds, where no thresholding has been applied to the data. Satellite-derived data for which precipitating clouds have not been filtered exhibit a similar seasonal behavior with systematically larger values (as suggested by the global annual mean shown in Table 1). An ocean-only cloud water average for CCM3 is also shown in the middle panel for more direct comparison with the satellite-derived data. It exhibits a slightly stronger seasonal cycle in cloud condensate, but is basically the same as the more complete global average. The all-sky representation of the satellite-derived data is more consistent with the averaging process used for the CCM3 simulated condensed water path since clear-sky conditions are also included in those averages. One important difference, however, is that cloud water is not differentiated from cloud ice in the CCM3 (i.e., the CCM3 data includes *total* condensate) and the Greenwald data includes only liquid condensate. The large discrepancy between the observational estimate and the CCM3 simulation of globally averaged cloud water is mostly attributable to differences in the Tropics and subtropics (as we will show later) for reasons that are not well understood. The physical reasons for the difference in the phase of the seasonal cycle are also difficult to understand, since ocean-only cloud water averages from the CCM3 exhibit the same kind of seasonal behavior as the more complete global average. Another way to try to indirectly explore the actual seasonal cycle in cloud water is to use the Earth Radiation Budget Experiment (ERBE) shortwave cloud forcing (SWCF) (bottom panel of Fig. 2). The increases in CCM3 SWCF during the Northern and Southern Hemisphere summer months are consistent with the increases in cloud water path shown in the middle panel. The fact that the ERBE SWCF data also indicate a similar seasonal behavior suggests that the annual cycle in cloud water path is likely to be more similar in phase to the CCM3 than to current satellite estimates of this quantity. The role of the partition between ice and liquid condensate in contributing to the

discrepancy in seasonal cycle requires further investigation.

Finally, we look at the annual cycle of evaporation, precipitation, and their difference ($E - P$), as averaged over land and ocean surfaces for both the CCM2 and CCM3. As seen in Fig. 3, the CCM3 exhibits systematically weaker evaporation and precipitation amounts over land and ocean surfaces when compared to the CCM2. Weak, but similar, seasonal variations in these quantities exist over ocean surfaces, whereas the two models show considerably different exchange characteristics over land surfaces. Both models show a seasonal cycle of evaporation over land maximizing during the Northern Hemisphere summer months. The amplitude of the CCM3 annual cycle is less than one-half as large as in the CCM2, and 40% smaller in terms of the annual amplitude. Land precipitation differences are equally large. The CCM3 shows little evidence for a strong annual cycle in precipitation, whereas the CCM2 shows a well-defined July maximum in precipitation, with a secondary maximum during April. As in the case of evaporation, precipitation over land is substantially reduced in the CCM3 when compared with CCM2, with maximum monthly average differences exceeding 1.5 mm day^{-1}. The simulated differences in evaporation and precipitation over land are largely attributable to the cloud optical property parameterization modifications (Kiehl 1994a; Hack 1998a) and to the incorporation of a considerably more realistic land surface treatment (Bonan 1996). The net result, as measured by $E - P$, is a noticeably weaker transfer of water from the oceans to the land in the CCM3 throughout the year. Both simulations show similar annual cycles in the land- and ocean-averaged $E - P$, where the ocean surplus and land deficit are systematically smaller in the CCM3.

3. Mean-state seasonal simulation properties

a. Temperature and specific humidity

Two of the most basic of all climate properties are the structure of the temperature and water vapor field. To interpret the simulation quality of these fields, we compare them to the National Centers for Environmental Prediction (NCEP) global reanalyses (Kalnay et al. 1996). The archive we use consists of twice-daily analyses at 17 pressure levels in the vertical from which 15-yr (1979–93) December–February (DJF) and June–August (JJA) climatologies were constructed. The results are truncated from T63 to T42 resolution for comparison to the pressure-interpolated fields from CCM3. Figures 4 and 5 show the CCM3 seasonal DJF and JJA zonal averages of temperature and specific humidity differences from the respective NCEP climatology.

Overall, the CCM3 simulation does a very credible job of reproducing the analyzed thermal structure, where the simulated temperatures are within 1–2 K of the analyzed field for the domain bounded by 50°N and 50°S
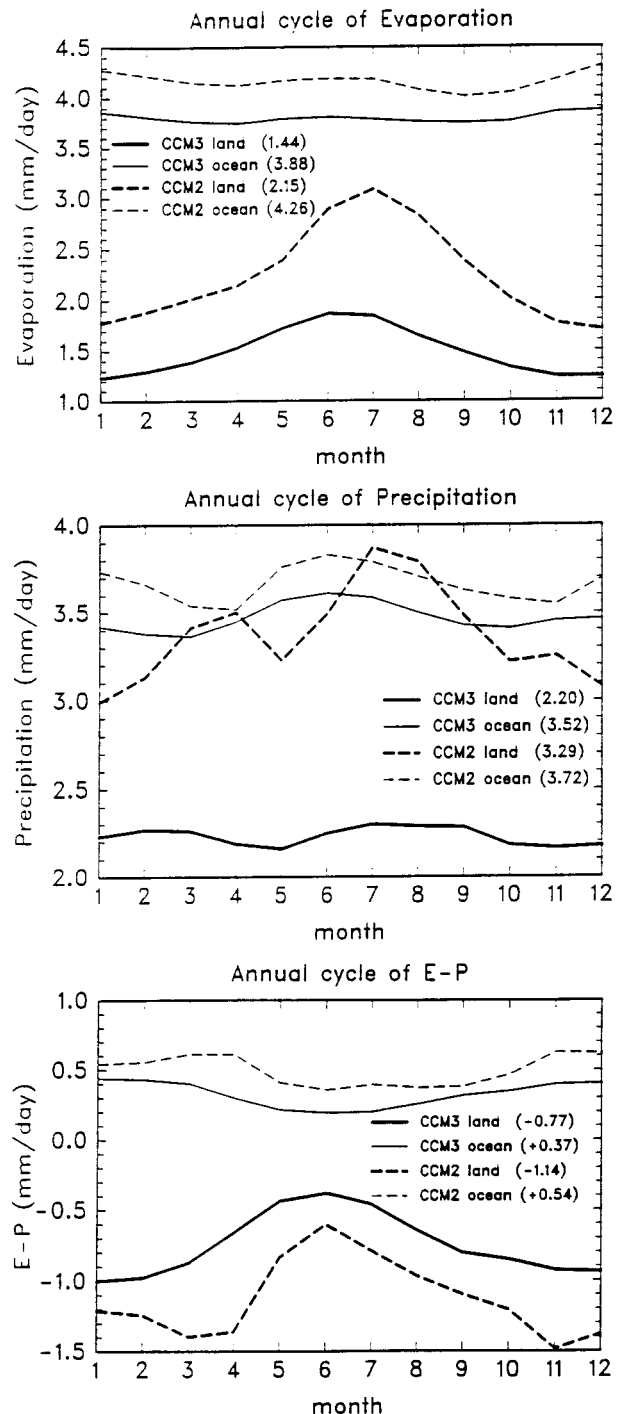

FIG. 3. Annual cycle of evaporation, precipitation, and $E - P$ averaged over land and ocean surfaces for the CCM3. Annual means are indicated in parentheses.

and 200 mb. The CCM3 simulation exhibits a weak warm bias in the low to middle portion of the tropical troposphere, as compared to the very weak cold bias seen in the CCM2. This warming of the Tropics accompanied the inclusion of the deep convection scheme. The
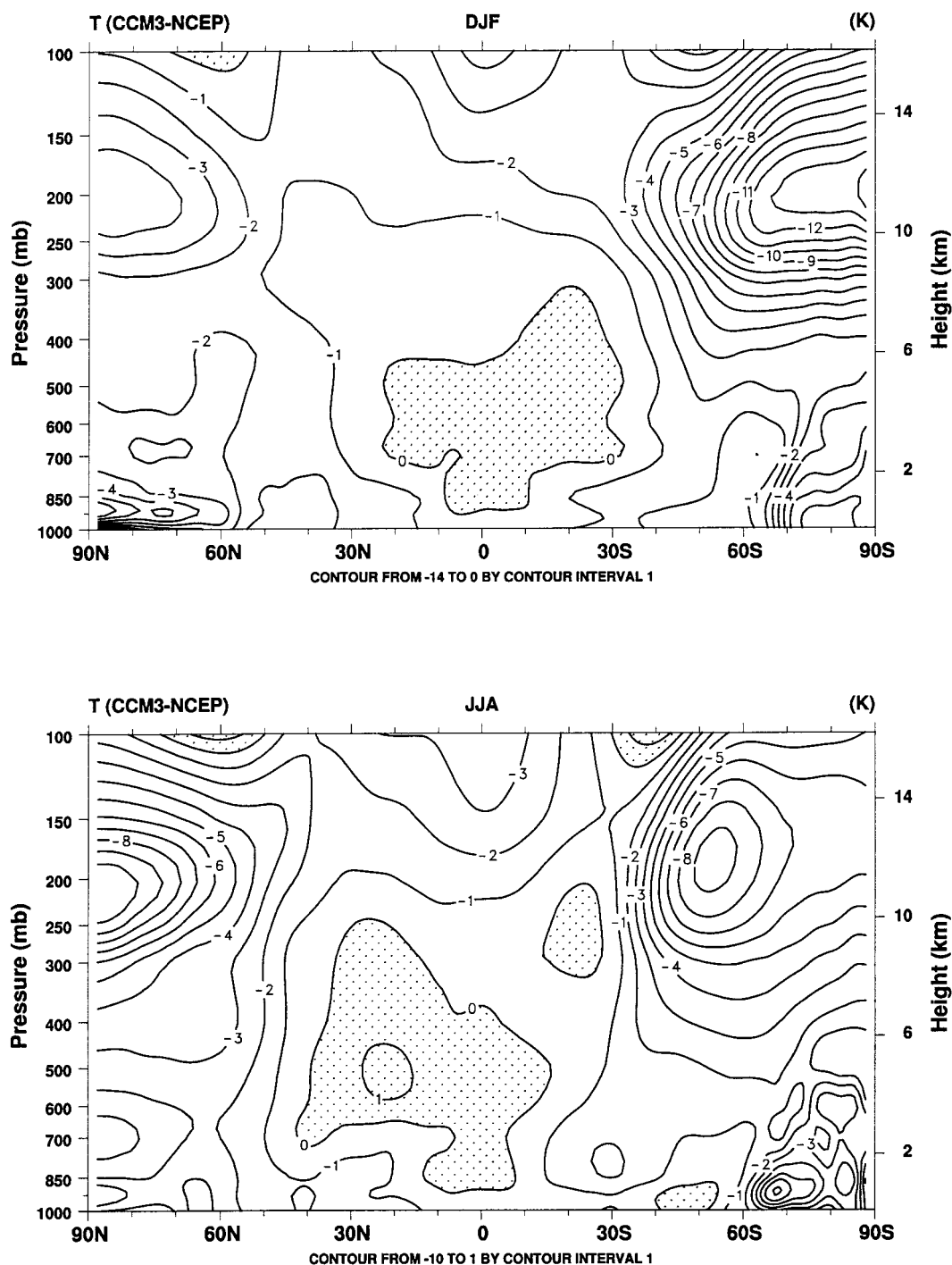
FIG. 4. Zonally and seasonally averaged differences in temperature (CCM3 − NCEP) for DJF and JJA.

CCM3 continues to poorly simulate polar tropopause temperatures, which can be from 10–14 K colder than analyzed. Cold polar tropopause simulations have been documented to be a pervasive problem in atmospheric general circulation modeling (Boer et al. 1992) and represents an ongoing simulation deficiency in the various versions of the NCAR CCM, despite the many other

major simulation improvements. Williamson and Olson (1998) have shown a marked improvement in the polar temperature bias, where the bias is reduced by more than a factor of 2, in response to the replacement of the CCM3 Eulerian dynamical core with a semi-Lagrangian dynamical core. Their results suggest that a large component of the CCM3 polar thermal bias may be attrib-
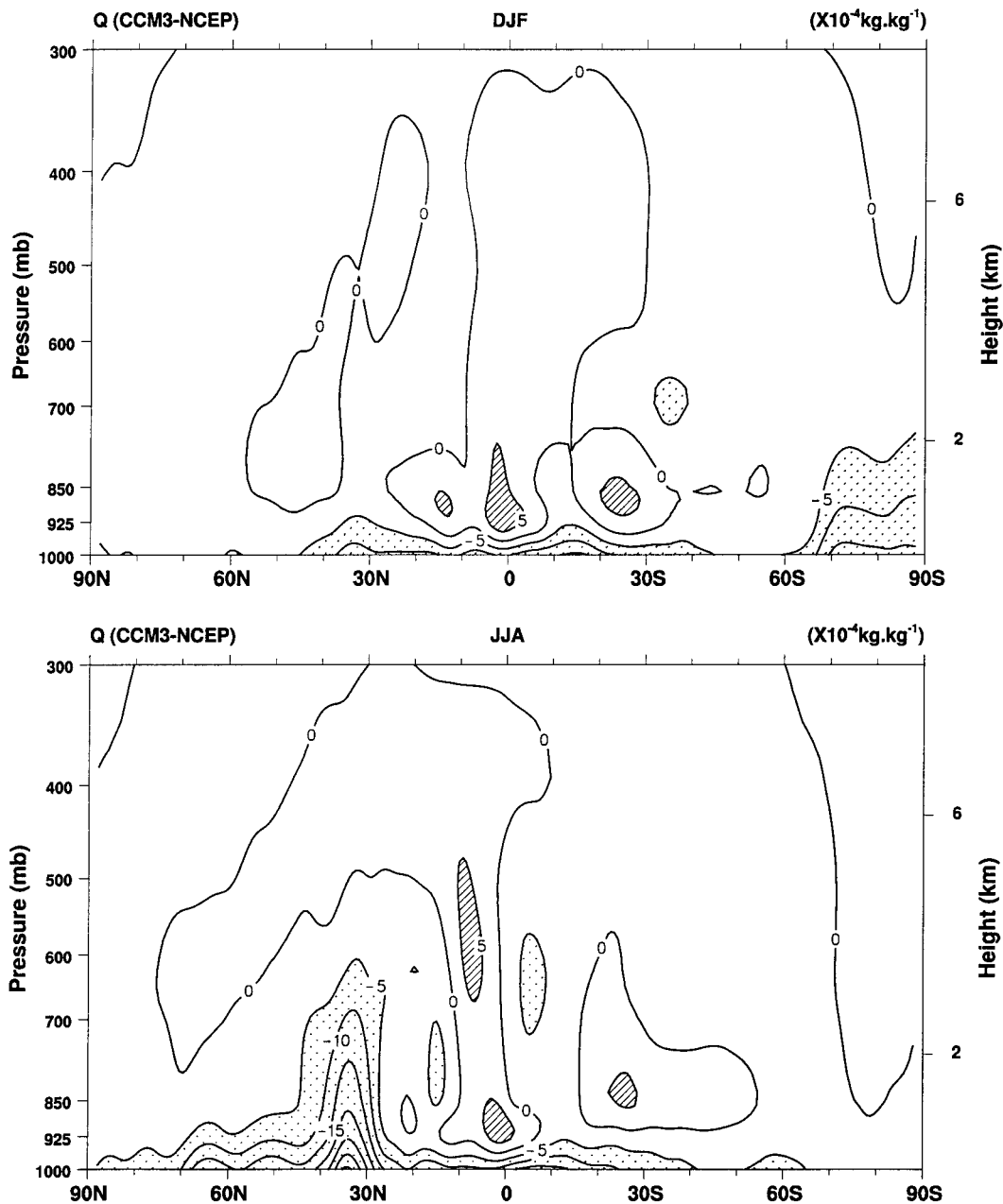
FIG. 5. Zonally and seasonally averaged differences in specific humidity (CCM3 − NCEP) for DJF and JJA.

utable to numerical approximation errors associated with large-scale advection. Tropical upper-troposphere temperatures are also more poorly simulated in the CCM3. Both seasons exhibit a zonal-mean cold bias of between 3 K and 4 K at the tropical tropopause. This type of cold bias was also seen in the CCM2 simulation, although it is more pronounced in the CCM3. The enhancement of this bias also accompanied the introduction of the deep convection scheme, and the associated increase in upper-level tropical cloud amount. Despite the problems with properly representing tropopause temperatures, the CCM3 does a very good job of cap-

turing variations in tropopause height. This attribute of the simulation is readily seen in zonally averaged temperature plots (not shown) and in regional thermodynamic profiles (which will be shown later).

The tropospheric warm bias present in the JJA CCM2 simulation poleward of 40°N has become a weak cold bias in the CCM3. The CCM2 Northern Hemisphere warm bias was primarily a consequence of inadequacies in the diagnosis of cloud optical properties, which contributed to an excessive input of solar energy at the surface. Improvements to the parameterization of clouds and radiation, along with the introduction of a more

realistic land surface model, addressed this very serious simulation deficiency. As in the CCM2, simulated temperatures at high latitudes in the lower troposphere continue to be colder than analyzed.

The zonally averaged cross sections of specific humidity differences shown in Fig. 5 are not as useful a measure of the simulation quality as are the temperature differences. There are large uncertainties in the analyzed moisture field (e.g., Trenberth and Guillemot 1995), where the water vapor distribution strongly depends upon the collection of parameterized physics associated with a particular analysis cycle. Consequently, these moisture biases are most useful for illustrating similarities in the behavior of the CCM3 against a standard analysis product, but should not be viewed as a definitive quantification of model error. For this reason we will also compare the simulated water vapor field with the NVAP climatology and with regional climatologies constructed from radiosonde data. When compared against the NCEP analysis, the CCM3 simulated moisture distribution appears to be in reasonably good agreement. There is evidence of a meridionally broad low-level dry bias on the order of 1 g kg^{-1} in both DJF and JJA, with a weak moist bias in the ITCZ. The largest difference appears poleward of 30°N during JJA where a pronounced dry bias extends up through the middle troposphere, with maximum values of 3.5 g kg^{-1} at 35°N near the surface. This dry bias is in sharp contrast with the CCM2 simulation, which exhibited a modest moist bias in this region, principally due to its cloud optical property deficiencies and relatively crude representation of land surfaces.

Because of the uncertainties in any single analysis of the water vapor field, we also compare the CCM3 with the NVAP precipitable water climatology, the vertical integral of the specific humidity. Figure 6 shows the zonal- and seasonally averaged precipitable water for CCM3, CCM2, NVAP, and NCEP. This figure shows a similar meridional bias in the JJA meridional distribution of water vapor, where a pronounced Northern Hemisphere dry bias is clearly indicated by the NVAP data, exceeding 5 kg m^{-2} (or 5 mm) over most of the region between the equator and 40°N (where NCEP is also dry when compared with NVAP). Note that the CCM2 simulation tended to be slightly more moist than the NVAP analyses in both seasons, with a moderate moist bias over the mid- to high latitudes of the Northern Hemisphere during JJA.

The horizontal distribution of precipitable water, and its difference from the NVAP dataset, are shown in Figs. 7 and 8 for DJF and JJA. The CCM3 produces relatively minor seasonal changes in the precipitable water distribution except over the Amazon basin, central Africa, and in the vicinity of the Indian subcontinent. These seasonal excursions of the meridional maximum in precipitable water are primarily responsible for the meridional shifts seen in the zonal mean. Despite relatively good agreement in the zonal-mean values, there are
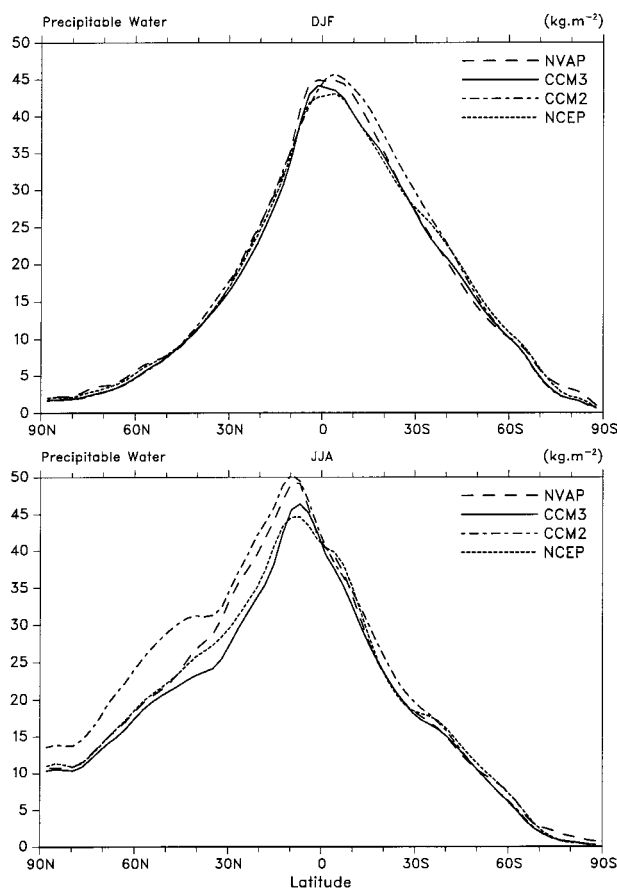

FIG. 6. Zonally and seasonally averaged precipitable water distribution for the CCM3 and CCM2 simulations, and for the NCEP and NVAP water vapor analyses.

some significant regional differences between the simulated water vapor field and NVAP. The DJF simulation shows a large spatially coherent dry region stretching from the southern Indian Ocean eastward through the South Pacific convergence zone (SPCZ), and a second feature extending across the equatorial Atlantic, Northern Africa, and into Northern India. These differences typically exceed 6 mm, representing approximately a 15%–20% error. Similar, but more severe, regional differences are seen in the JJA simulation. The atmosphere over warm continental surfaces appears to be systematically dry, exceeding 10 mm over large areas, where these differences represent local errors of 30% or more. Even oceanic regions exhibit a significant dry anomaly, as seen in JJA over much of the western Pacific.

The structure and magnitude of the precipitable water errors shown in Figs. 6–8 depend very strongly on the particular analysis product used to represent the real atmosphere. For example, the differences between the NCEP analyses, ECMWF analyses, and NVAP climatology can produce similar patterns to what is seen in Figs. 7 and 8. Another way to help verify the characteristics of systematic errors in temperature and moisture
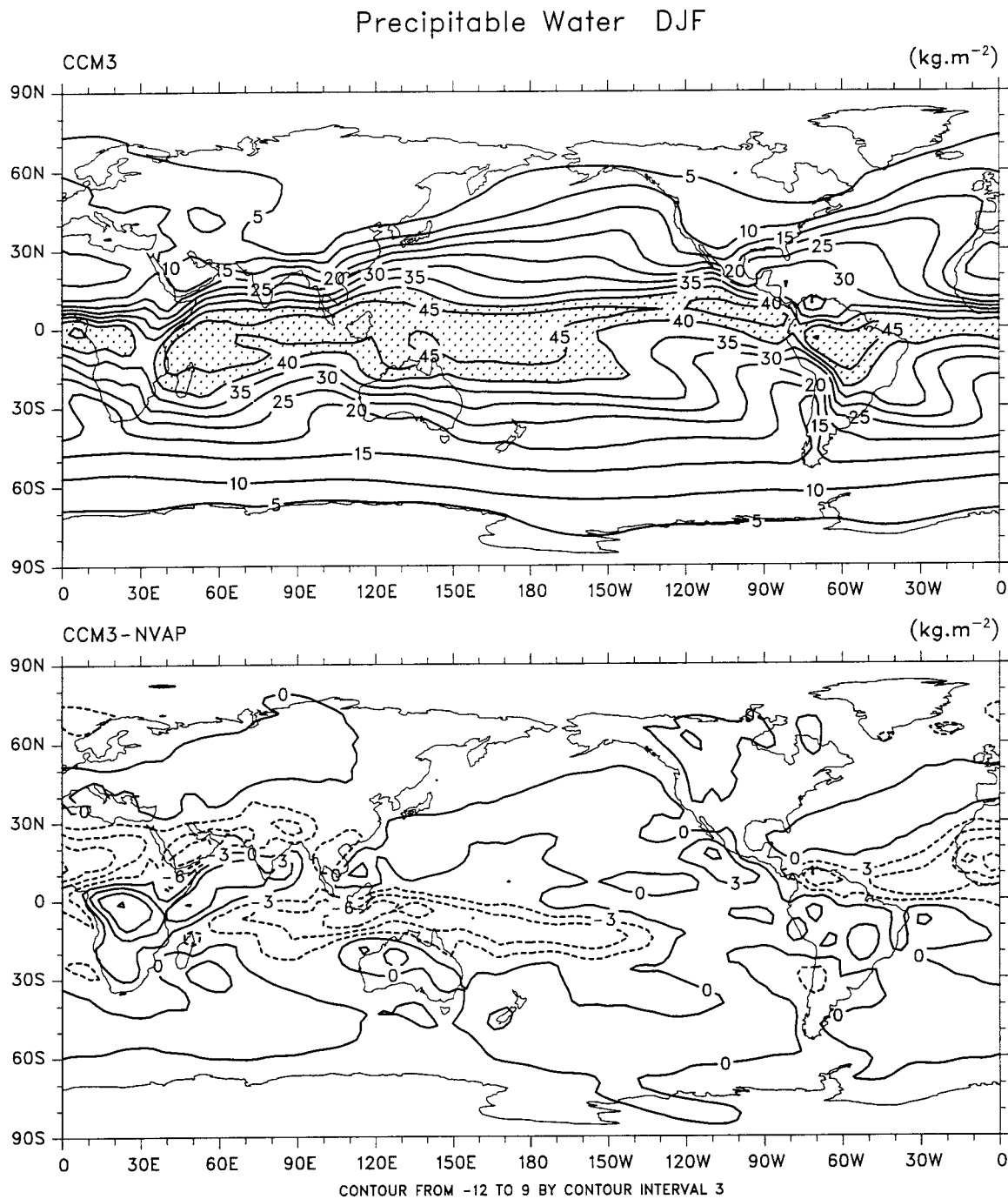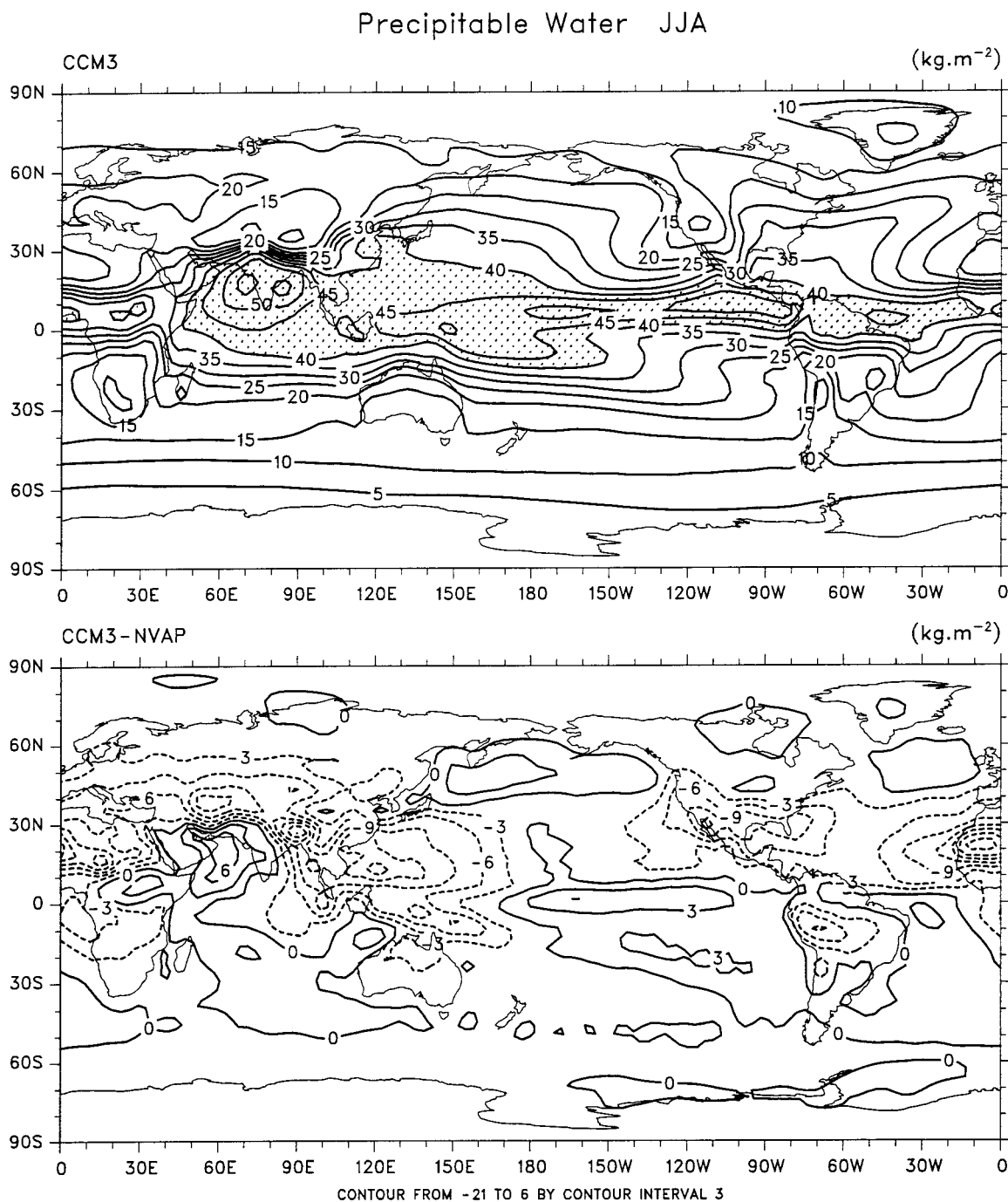
Precipitable Water DJF

FIG. 7. Global distribution of precipitable water as simulated by the CCM3 for DJF (top panel) and the difference with respect to the NVAP analysis.

in the simulation is to compare vertical thermodynamic profiles produced by the model with in situ radiosonde measurements at locations having long, high quality, observational records. This is typically done for approximately 50 sites as a part of model development activity, where we present results from two of them. Since the more severe moisture biases tend to be confined to the Tropics and midlatitudes, we have selected locations representing midlatitude ocean, and tropical western Pacific climates. The two sites, which were previously used to evaluate the quality of the CCM2 thermodynamic simulation (Hack et al. 1994), are centered over the Azores (38.7°N, 27.1°W) and the Yap Atoll (9.4°N, 138.1°E). The Azores radiosonde data makes

Precipitable Water   JJA

FIG. 8. Global distribution of precipitable water as simulated by the CCM3 for JJA (top panel) and the difference with respect to the NVAP analysis.

use of a single reporting station, while the Yap soundings incorporate two radiosonde stations. Profiles of temperature and specific humidity are shown in Figs. 9 and 10 for the months of January and July, respectively. The climatological observational record is given at discrete locations in the vertical where the dots represent the long-term average and the error bars indicate one

standard deviation with respect to observed interannual variability. The CCM3 temperature and specific humidity data are shown on the same diagrams by the solid line.

The overall quality of the CCM3 simulated thermodynamic structure at these two sites is mixed. The January lower to midtropospheric temperature structure is
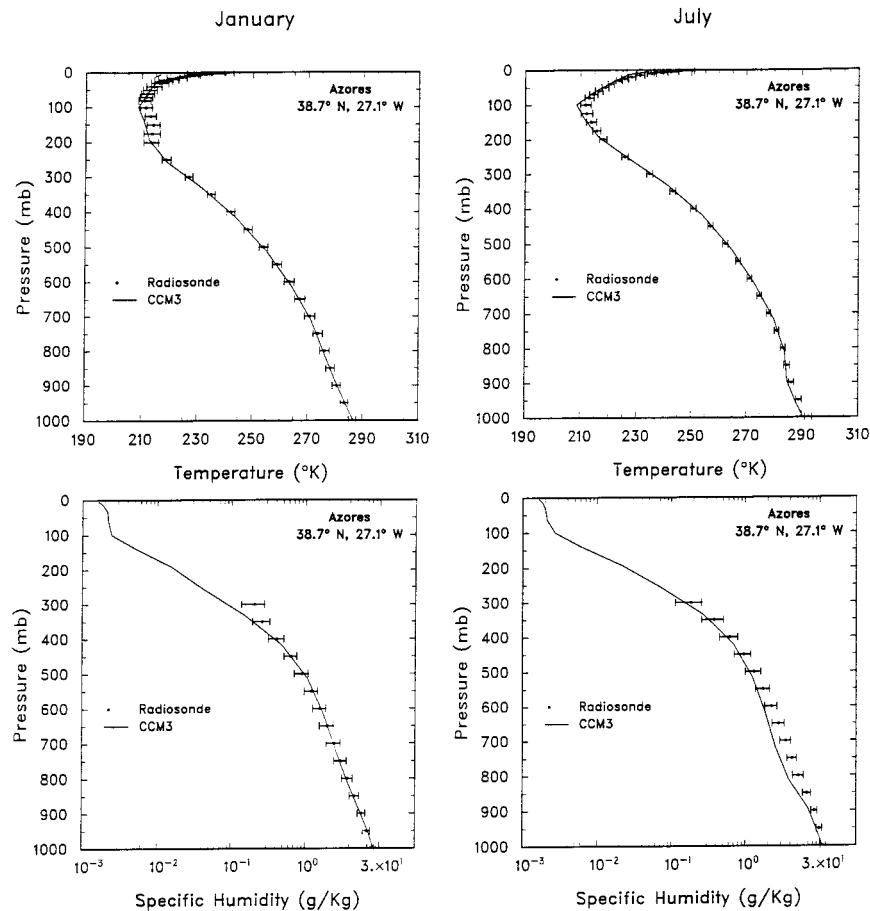
January

July

FIG. 9. Vertical climatological profiles (January and July averages) of temperature and specific humidity for the CCM3 and radiosonde observations over the Azores.

improved at both sites, eliminating the weak cold bias exhibited by the CCM2 (see Fig. 11; Hack et al. 1994). However, simulated tropopause temperatures are colder than observed, despite the fact that tropopause heights are well represented. The January water vapor distribution over Yap is quite dry in the low to midtroposphere and too moist in the upper troposphere. During July, the temperature structure over the Azores represents an overall improvement when compared to CCM2, reducing a mid- to upper-tropospheric warm bias and a more severe cold bias at the tropical tropopause. The Yap temperature profile shows warmer than observed values in the middle troposphere and a cold bias at the tropical tropopause. The more serious thermodynamic deficiencies occur in the July water vapor profiles, where both sites are severely dry between the top of the atmospheric boundary layer and middle troposphere. Other radiosonde sites suggest that the form of this moisture bias is a fairly widespread characteristic of the CCM3 water vapor distribution. The vertical distribution of the anomaly, dry lower troposphere, and moist upper troposphere is a signature of the deep convection scheme, and is perhaps the most serious degradation of the

CCM3 simulation when compared to the CCM2, for which the July water vapor structure was very well reproduced in the Tropics.

A concise characterization of the simulated thermodynamic structure is the vertical profile of equivalent potential temperature, a measure of the atmospheric moist static stability. Figure 11 illustrates the January and July θ_e distributions at the Azores and Yap sites for the CCM3, CCM2, and radiosonde observations. The overall improvement in the January Azores profile is quite remarkable, as is the improved simulation of the mid- to upper troposphere during July. As suggested by Figs. 9 and 10, however, the lower-tropospheric profile of θ_e is markedly degraded for the Yap profiles in both seasons, and for the July Azores profile. The Yap profiles also show θ_e anomalies associated with a warm and moist bias between 200 and 400 mb.

b. Cloud water

It is widely accepted that clouds (i.e., water in condensed form) exert an important forcing on the climate system as a regulator of the radiative heating field. The
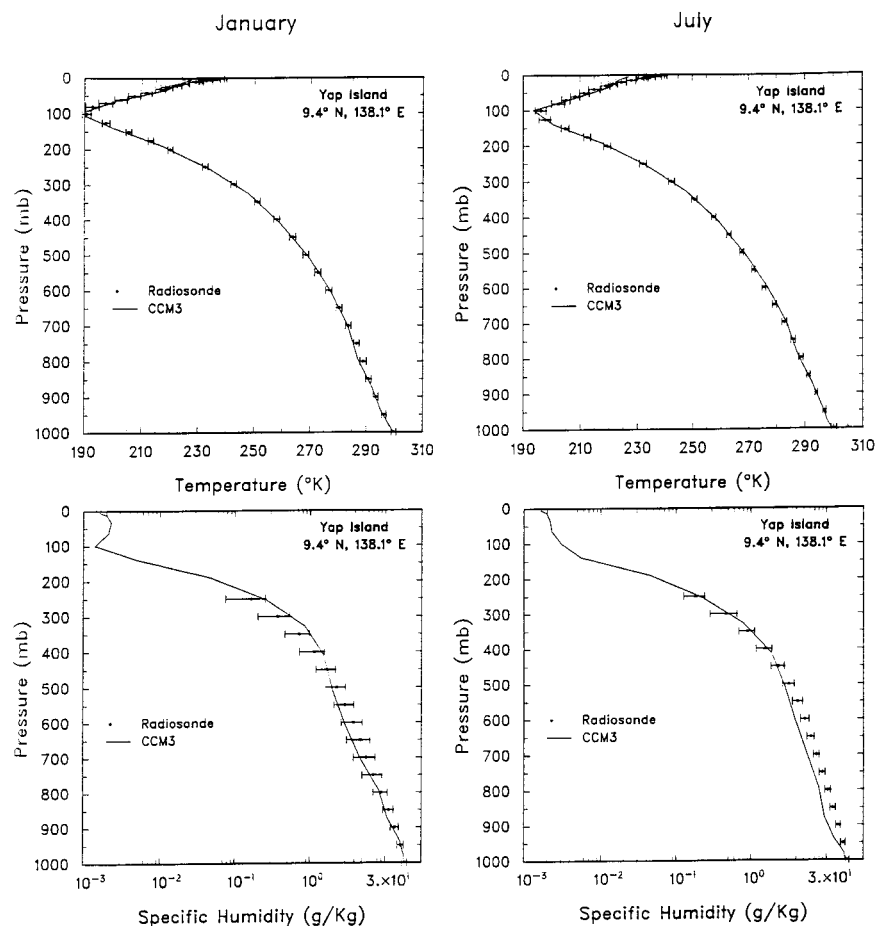
January

July

FIG. 10. Vertical climatological profiles (January and July averages) of temperature and specific humidity for the CCM3 and radiosonde observations over the Yap Atoll.

global magnitude of this cloud forcing is shown in Table 1 for both the shortwave and longwave portions of the TOA radiation budget. Ironically, cloud processes are a very poorly understood aspect of the climate system, representing one of the principal sources of uncertainty in the modeling of global climate (e.g., Cess et al. 1990). Cloud parameterization schemes are either diagnostic, for which cloud properties are parametrically derived from large-scale state information, or prognostic, which introduce additional large-scale state variables to represent the cloud field. The CCM3 cloud parameterization scheme is a diagnostic approach, where both cloud amount and the corresponding cloud optical properties are simply evaluated from several other large-scale properties of the simulated flow field (Kiehl 1994a; Hack 1998a; Kiehl et al. 1998a). Even though cloud water is not carried as a prognostic variable in the CCM3, it strongly influences the simulated global and regional energy budgets (Kiehl et al. 1998b). The climatological distribution of cloud water is therefore worthy of some discussion.

The first thing to note about condensed water in the atmosphere is how remarkably small it is when com-

pared to water stored in vapor form (see Table 1). The CCM3 simulated global annual mean of 46.5 g m^{-2} is around 500 times smaller than the analogous value for precipitable water, yet is of comparable climate importance in terms of modulating the global radiation balance, the so-called clouds and climate problem (e.g., Wielicki et al. 1995; Kiehl 1994b). Zonally and seasonally averaged distributions of condensed water path are shown in Fig. 12 for the CCM3, and for the satellite-derived values (ocean only) of Greenwald et al. (1995) and Weng and Grody (1996). The Greenwald data include the 4-yr period 1988–91 and represent an *all-sky* field of view, where the contributions of precipitating clouds to the liquid water path have been filtered (since liquid water path retrievals are unreliable when precipitation is present). The Weng and Grody data include the 9-yr period 1988–96. As mentioned earlier, the CCM3 results include both water and ice condensate, while the Greenwald data, and Weng and Grody data, are for liquid clouds only.

The CCM3 results exhibit well-defined condensed water maxima in the extratropical storm tracks, along with a very weak secondary maximum (only during
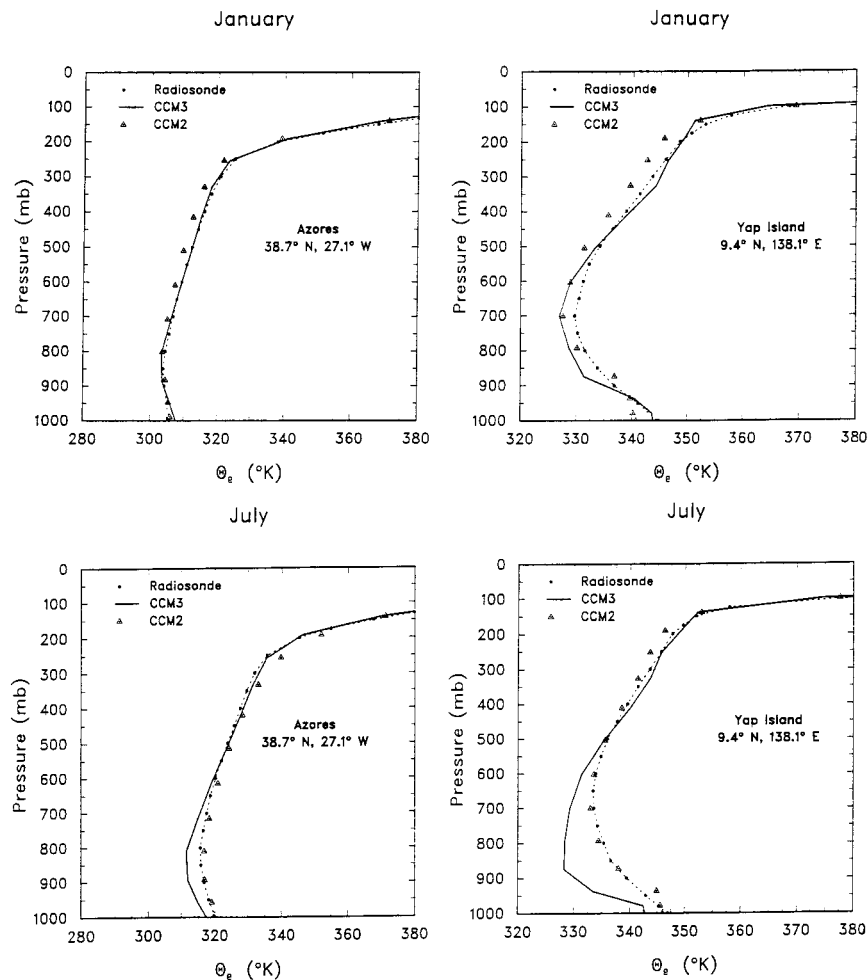
FIG. 11. Vertical climatological profiles (January and July averages) of equivalent potential temperature for the CCM3, CCM2, and radiosonde observations over the Azores and Yap Atoll.

JJA) associated with the ITCZ. The satellite-derived cloud water path shows a very different meridional distribution, where both datasets show an obvious maximum in the ITCZ. The Greenwald data shows little meridional definition of extratropical features, while the Weng and Grody data exhibits better meridional separation, mostly due to pronounced minima in subtropical cloud water amount. The Southern Hemisphere extratropical maximum seen in the simulated data is essentially nonexistent in the satellite data. The lack of extratropical maxima in the satellite retrievals may be related to the absence of column-integrated ice condensate. The amplitude of the satellite-derived cloud liquid water path is also systematically larger than what is simulated by the CCM3 for the region bounded by 40°N and 40°S (where the zonally averaged satellite retrievals including precipitating clouds show an additional 20%–25% increase in magnitude). This discrepancy is particularly large in the ITCZ where both satellite datasets show cloud water amounts that are two to three times

the total condensate diagnosed by the CCM3. The seasonal behavior of the simulated zonal average of condensed water shows a strong seasonal oscillation in magnitude at the high latitudes, where the summer hemispheres contain 40% or more cloud condensate than in their respective winter season. The Greenwald satellite estimate also suggests a similar seasonal oscillation, but mostly for the Northern Hemisphere.

The DJF and JJA meridional distributions of total cloud amount are shown in Fig. 13 for CCM3, ISCCP, and *Nimbus-7*. These curves show a clear meridional shift in the seasonal location of the ITCZ and subtropical cloud features, but little evidence for large extratropical changes in total cloud fraction. In regions where total cloud fraction does exhibit large seasonal changes (e.g., the subtropics), the simulated cloud water path only weakly reflects the change in cloud amount. Thus, the zonally averaged cloud water path does not appear to be strongly correlated with more subjective measures of condensed water, such as total cloud amount. Never-

Zonal DJF Average Cloud Liquid Water Path

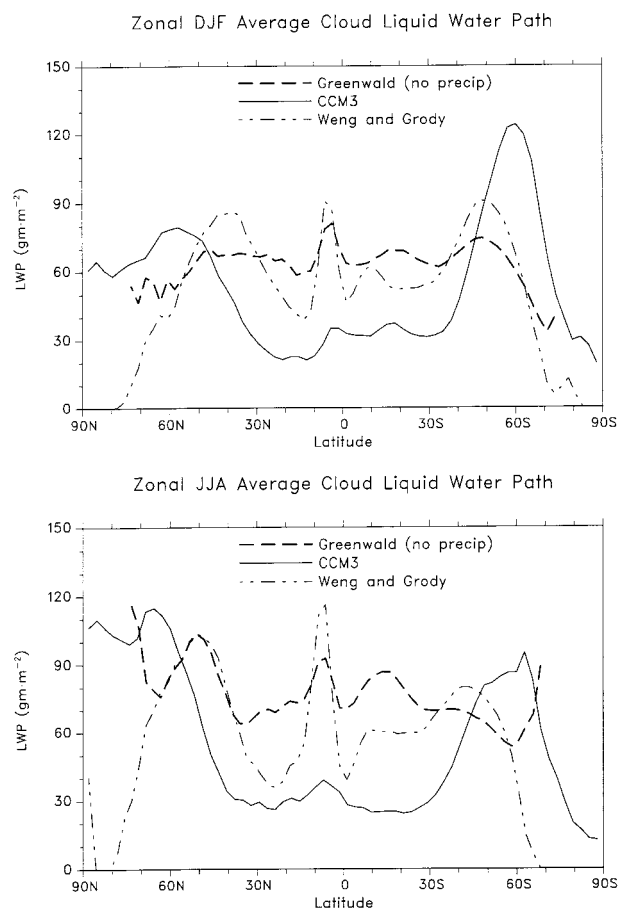Zonal JJA Average Cloud Liquid Water Path

FIG. 12. Zonally and seasonally averaged cloud water path (DJF and JJA) for the CCM3, Greenwald et al. (1995), and Weng and Grody (1996) cloud water climatologies.

FIG. 13. Zonally and seasonally averaged total cloud amount (DJF and JJA) for the CCM3, ISCCP, and *Nimbus-7*.

theless, the CCM3 cloud amount does show reasonably good agreement with the observational estimates, particularly the *Nimbus-7* climatology. We note that the local agreement between all three cloud fraction datasets is strongest for the JJA ITCZ, the same region where the CCM3 cloud condensate is most different from the corresponding satellite-derived cloud water estimates.

Figure 14 shows the DJF and JJA global distribution of condensed water path for the CCM3 simulation. The extratropical storm tracks are clearly defined in these figures, as are the dry subsidence regions in the subtropics (identified by well-defined minima in the cloud water distribution). Condensed water path generally exceeds 100 g m^{-2} in the storm tracks, where maximum values exceeding 150 g m^{-2} occur during the respective summer season (e.g., Gulf of Alaska during JJA). Dry desert regions, such as over the southwestern United States, northern Africa, and the high deserts over the interior of Eurasia are also easy to identify in both panels. Surprisingly, the ITCZ and other climate features associated with deep cumulus convection are only weakly represented. The strongest ocean features are seen in the eastern ocean basins, in particular, the eastern trop-
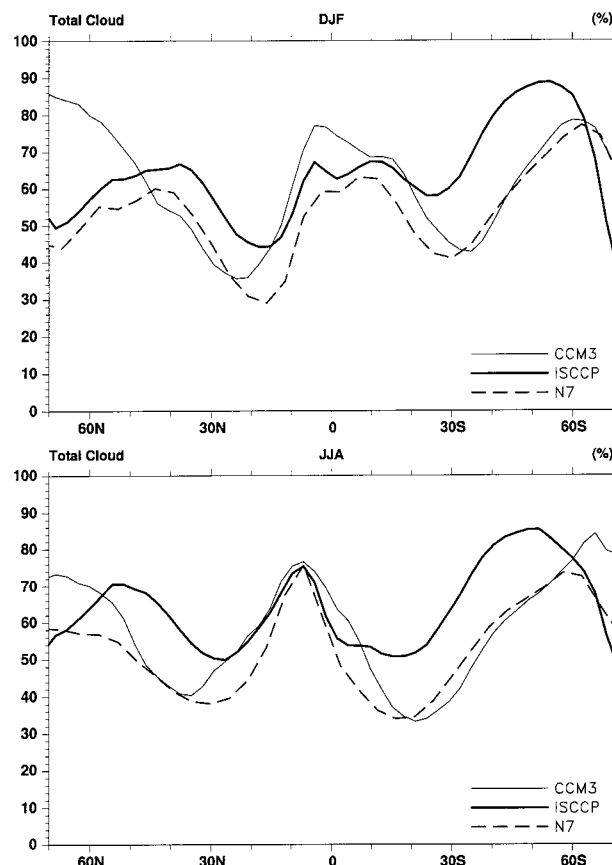
ical Pacific. This is in sharp contrast to the observational estimates of cloud water path, such as Greenwald et al. (1995) and Weng and Grody (1996), which show well-defined cloud water structures associated with the ITCZ. This is indeed an unexpected result, given the strong agreement in the TOA radiation budget between the CCM3 and ERBE observations (Kiehl et al. 1998b). Since the satellite-derived data does not include cloud ice, the actual differences are likely to be even larger than suggested by Fig. 12. The reasons for such large differences between lower-latitude simulated and satellite-derived cloud water path are not well understood and are a topic for additional research. For example, despite the more realistic representation of the cloud field optical properties in CCM3, the low-latitude discrepancy between observed and CCM3-simulated condensed water remains similar to what was seen in CCM2 (Hack 1998a). This type of discrepancy presents an interesting scientific opportunity to better understand the relationship between large-scale observational estimates of cloud water (e.g., subgrid-scale variability issues related to retrieval) and the treatment of parameterized radiative transfer (e.g., modeling assumptions related to the cloud field; anomalies in cloud absorption) in atmospheric general circulation models (AGCMs).
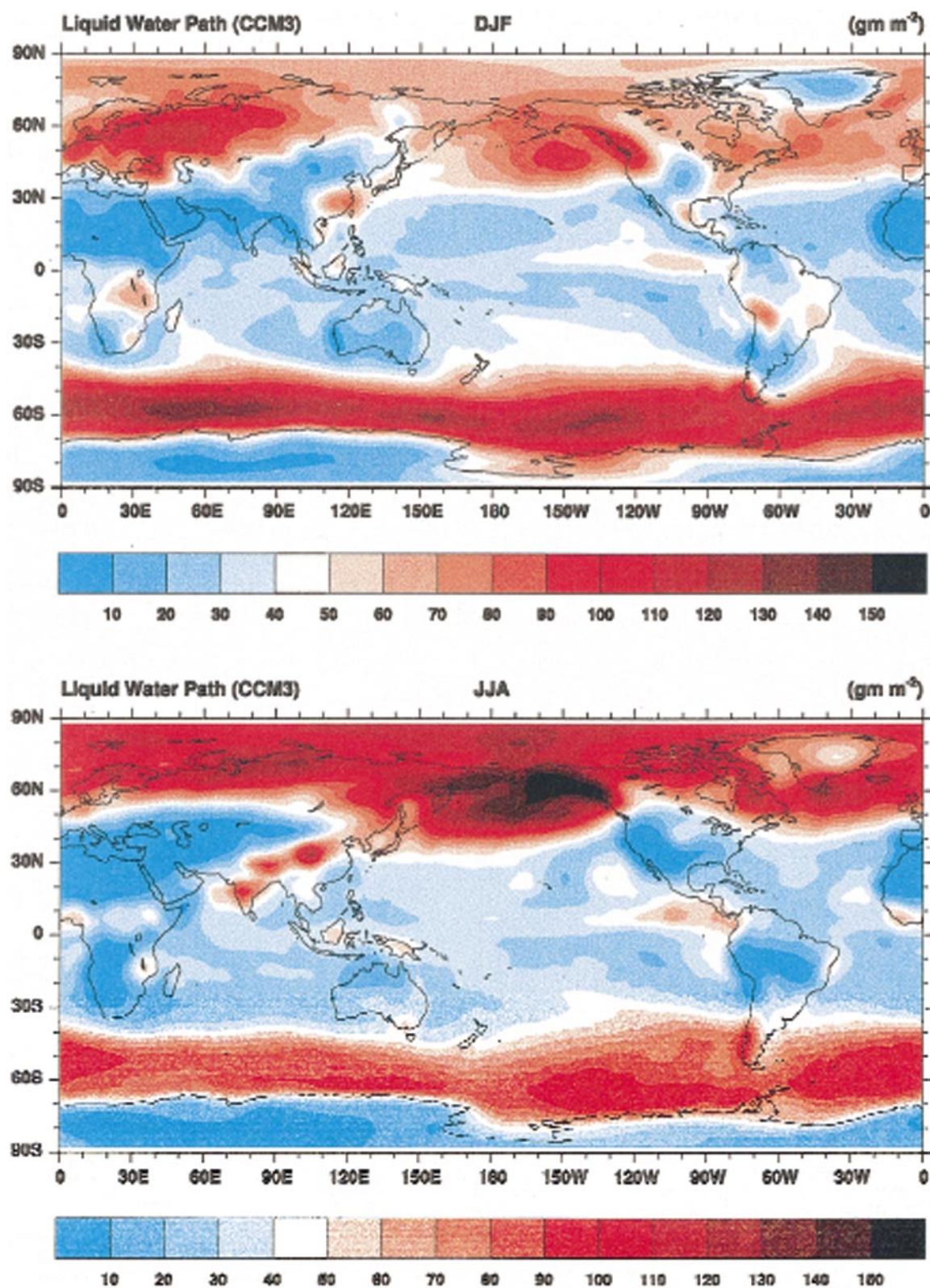
FIG. 14. Global seasonal distribution of cloud water path as simulated by the CCM3 for DJF (top panel) and JJA (bottom panel).
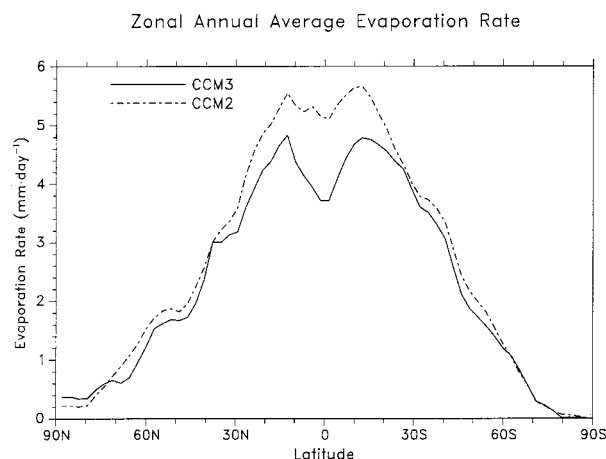
FIG. 15. Zonally and annually averaged evaporation rate for the CCM3 and CCM2.

FIG. 16. Zonally and annually averaged precipitation rate for the CCM3, CCM2, and Xie and Arkin (1996) precipitation climatology.

c. Evaporation and precipitation

The evaporation and precipitation fields illustrate the properties of water exchange between the atmosphere and the underlying surface. The zonal- and annually averaged evaporation rate is shown in Fig. 15 for the CCM2 and CCM3 (where a comparable *global* observational dataset does not exist). The evaporation curves clearly show that the most vigorous transfer of water to the simulated atmosphere occurs in the subtropics. This feature is particularly obvious for the CCM3 simulation, which exhibits well-pronounced evaporation maxima near 20°N and 20°S. Overall, the CCM3 evaporation rates are significantly and systematically weaker than for the CCM2. The suppression of surface evaporation is especially obvious in the deep Tropics, where it is reduced by more than 1.4 mm day^{-1} ($\sim$40 W m^{-2}). This enhanced suppression of evaporation in the vicinity of ITCZ convection is a more realistic feature of the CCM3 simulation, showing good agreement with corresponding oceanic estimates (e.g., see Oberhuber 1988; Doney et al. 1998; Kiehl 1998).

The zonal- and annually averaged precipitation rate is shown in Fig. 16 for the CCM2, CCM3, and the Xie and Arkin (1996) analysis. The precipitation distribution also shows a systematic reduction when compared with CCM2 and is more consistent with the Xie and Arkin estimates. Most notable is that the magnitude of extratropical reductions in precipitation are on par with precipitation changes in the ITCZ. The zonally and annually averaged net surface exchange of water, $E - P$, is shown for CCM2 and CCM3 in Fig. 17, and expressed in energy units (where 1 mm day$^{-1} \sim$ 29.055 W m^{-2}). The regions 10°–40°N and 10°–40°S are well-defined source regions of total water, where the deep Tropics and extratropics represent regional sinks of total water. The ITCZ water sink is much broader and more symmetric about the equator in the CCM3 simulation, where very large differences along and just south of the equator
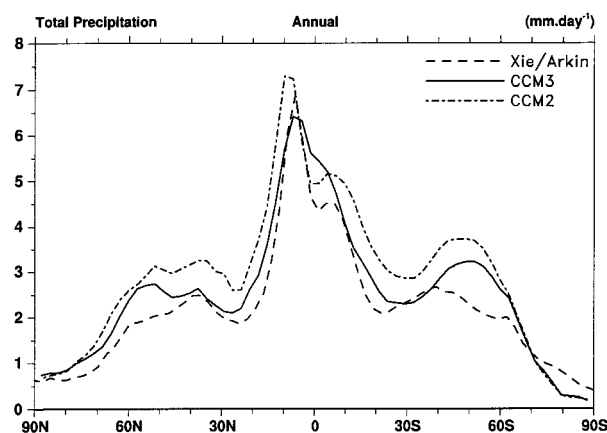
are a consequence of both reduced evaporation and increased rainfall. The implied meridional export of water from source regions to sink regions is quite different for the two models, where the Southern Hemisphere subtropics are the principal source of water powering the atmospheric hydrologic cycle in the CCM3.

As seen in the annual mean, the CCM3 exhibits a systematic decrease in evaporation for both seasons when compared to the CCM2 (Fig. 18), where the more significant extratropical differences occur in the Northern Hemisphere during JJA (in response to changes in cloud optical properties, land surface representation, and boundary layer formulation). The most noticeable response when comparing CCM3 to CCM2 is the pronounced reduction of evaporation in the ITCZ region, a signal clearly associated with the introduction of the Zhang–McFarlane deep convection scheme. The suppression of evaporation rates elsewhere in the subtropics and extratropics is a simulation response primarily associated with changes to the atmospheric boundary layer
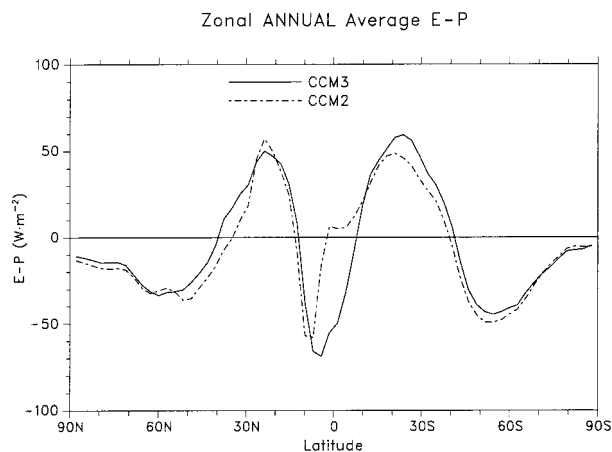

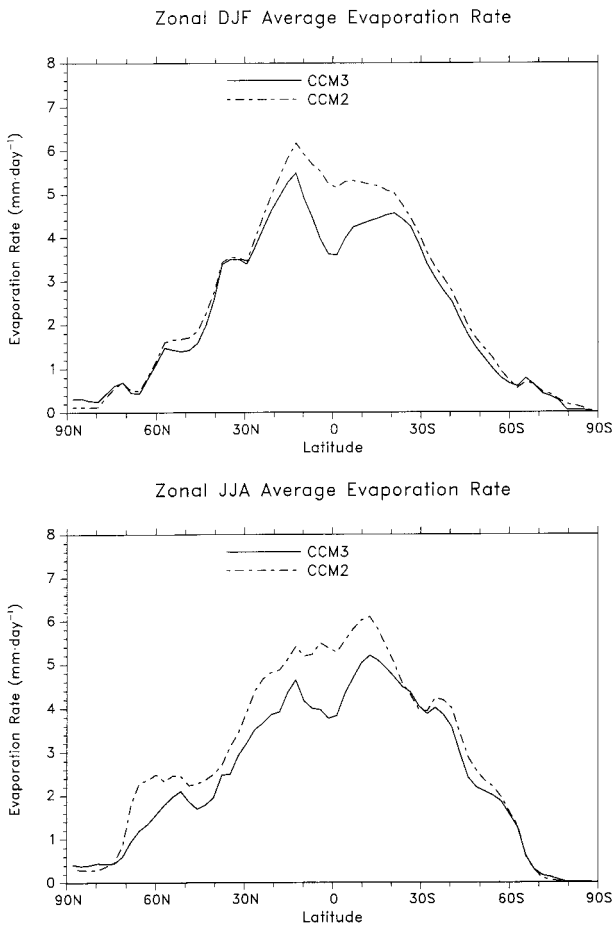FIG. 17. Zonally and annually averaged $E - P$ for the CCM3 and CCM2.

FIG. 18. Zonally and seasonally averaged evaporation rate (DJF and JJA) for the CCM3 and CCM2.

FIG. 19. Zonally and seasonally averaged precipitation rate (DJF and JJA) for the CCM3, CCM2, and Xie and Arkin (1996) precipitation climatology.

formulation. The seasonal zonal averages of precipitation (Fig. 19) show considerably greater differences between the CCM2 and CCM3 than suggested by the annual mean. Seasonal maxima in ITCZ precipitation are substantially reduced and are more consistent with the Xie and Arkin climatology. Although reduced in amplitude, simulated precipitation rates in the midlatitude storm track regions continue to be slightly higher than in the observational estimates. Two features worth noting are the improvement in the simulation of the Southern Hemisphere subtropical minimum during JJA, and the anomalous shift in the DJF ITCZ maximum more than 10° north of both the Xie and Arkin and CCM2 locations. These panels show a clear tendency for the simulated tropical precipitation maximum to remain in the Northern Hemisphere year round, in sharp contrast with most observational estimates, which suggest a seasonal migration of ITCZ precipitation across the equator. The large changes to both evaporation and precipitation produce large differences in the seasonal distribution of the net water exchange at the surface between the CCM3 and its predecessor model (see Fig. 20). The CCM3 simulates a considerably weaker sea-
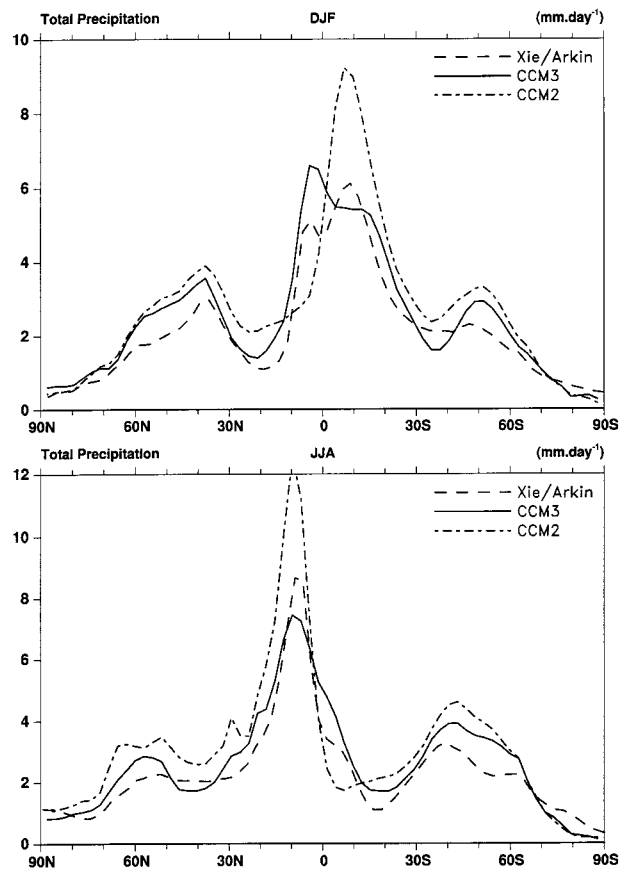
sonal meridional excursion of the net water sink in the deep Tropics, largely due to the weak seasonal migration of ITCZ precipitation. The subtropical water source region in the winter hemispheres is much weaker as well, mostly due to a reduction in meridional extent. Also note the relatively large Northern Hemisphere extratropical differences, which are mostly attributable to changes in the total water exchange over land surfaces.

Figures 21 and 22 show the DJF and JJA global distribution of precipitation for the Xie and Arkin climatology and the CCM3 simulation. Overall, the CCM3 does a very credible job of simulating the principal features of the observed precipitation distribution. The Northern Hemisphere DJF extratropical storm tracks are especially well represented, as is the general pattern of tropical precipitation. Note that the seasonal behavior of extratropical precipitation in both hemispheres, exhibiting enhanced storm track precipitation in the winter hemisphere, is well simulated by the CCM3. Low precipitation rates in the subtropics with well-defined minima in the eastern oceans are realistically represented. The southeast Asian monsoon is particularly well reproduced, representing one of the more notable simulation improvements when compared to the CCM2. The
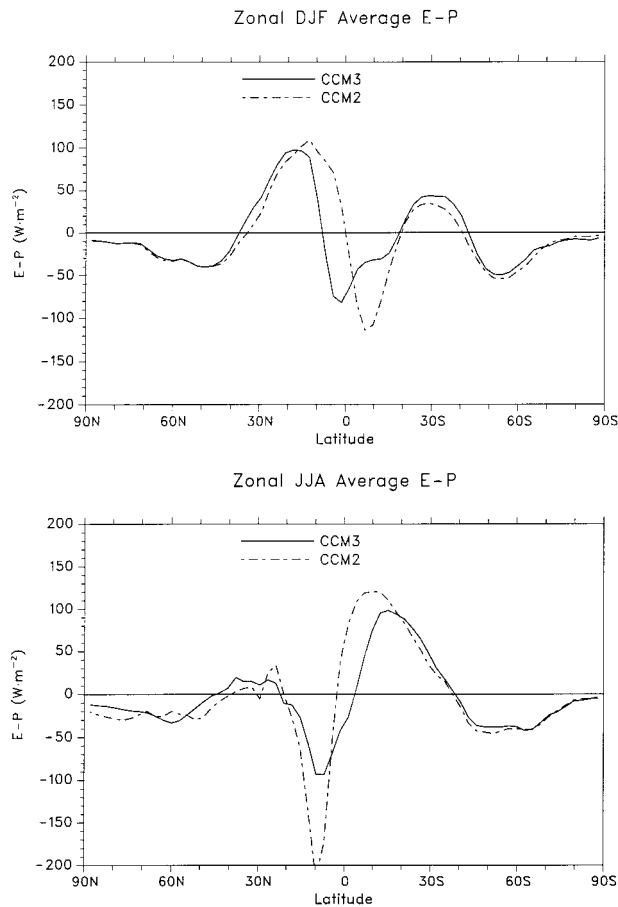
Zonal DJF Average E−P

Zonal JJA Average E−P

FIG. 20. Zonally and seasonally averaged $E − P$ (DJF and JJA) for the CCM3 and CCM2.

into the Caribbean, with weaker than observed precipitation in the eastern Atlantic. There is also an anomalous precipitation maxima over the Arabian Peninsula, an unrealistic meridional separation of the ITCZ in the west-central Pacific, and an anomalous precipitation maxima in the north subtropical central Pacific. The CCM3 exhibits more of a tendency to form double ITCZ structures, as suggested by both the DJF and JJA seasonal means. This characteristic appears to be an attribute of the deep convection scheme, which tends not to maintain deep convective structures along the equator. Despite these deficiencies, the overall simulation of precipitation represents a notable improvement when compared with the CCM2.

The simulated evaporation field is shown in Fig. 23 for DJF and JJA. Both seasons show a clear evaporation minimum in the ITCZ, with extensive regions of high evaporation in the respective winter hemispheres. The DJF distribution shows evaporation maxima in the Northern Hemisphere western oceans (along the Kuroshio and Gulf Stream currents) as well as in the western Arabian Sea, all well exceeding 8 mm day^{-1} (~240 W m^{-2}). Another extensive region of high evaporation is located in the subtropical western Pacific, providing much of the moisture supply for the convective features to the south and west. A relatively small, but vigorous region of high evaporation is seen in the eastern Pacific, to the north and east of the anomalous convective activity discussed in Fig. 22. Significant evaporation rates are also seen over much of South America and Southern Africa. During JJA, an extensive and coherent region of high evaporation stretches across the southern oceans, with maximum rates occurring in the Southern Indian Ocean. Other significant features are present in the east-central subtropical Pacific, the western subtropical Atlantic, and in the Arabian Sea just south of the anomalous convective activity over the Arabian Peninsula. Large evaporation rates are also seen over the north-central and southeastern parts of the United States, India, and large portions of southeast Asia.

The evaporation field shows a distinct minimum along the equator in the vicinity of deep ITCZ convection in both seasons. This characteristic represents a significant improvement when compared with CCM2, which only weakly captured the observed equatorial minimum (e.g., see Fig. 15). The reduction in evaporation is of particular importance to the simulation of a realistic surface energy budget over the tropical western Pacific warm pool (e.g., see Kiehl 1998), where observational estimates suggest tropical evaporation reaches a relative minimum. This east–west gradient in evaporation over the western tropical Pacific is reasonably well represented by the CCM3, and is particularly obvious in the JJA distribution.

The net water exchange with the surface, $E − P$, is shown in Fig. 24. The major tropical precipitation features are clearly visible, with local water deficits exceeding 300 W m^{-2} (~10 mm day^{-1}) in the long-term

areal extent of the monsoon precipitation into northern India and south into the southern Indian Ocean, with a well-defined maximum in the Bay of Bengal, is well captured in the simulation. The overall pattern of precipitation exhibits a more coherent and spatially smooth structure when compared to the CCM2, and better resembles the Xie and Arkin precipitation distribution and amplitude characteristics. Nevertheless, a number of significant biases are apparent in the simulated seasonal structure. The DJF pattern shows an anomalous precipitation maximum in the western tropical Pacific, positioned well north of the observed precipitation maximum (which is also seen as a TOA radiative anomaly). Vigorous ITCZ convection extends too far east in the Pacific Ocean, and convection in the Indian Ocean is positioned too far to the north with evidence of a double ITCZ not reflected in the observational data. Western Pacific convection extends too far south into northwestern Australia, and there is a tendency to lock precipitation over the Andes Mountains, a problem that plagues many other AGCMs, including the CCM2. The JJA distribution shows excessive convective activity over Central America erroneously extending eastward
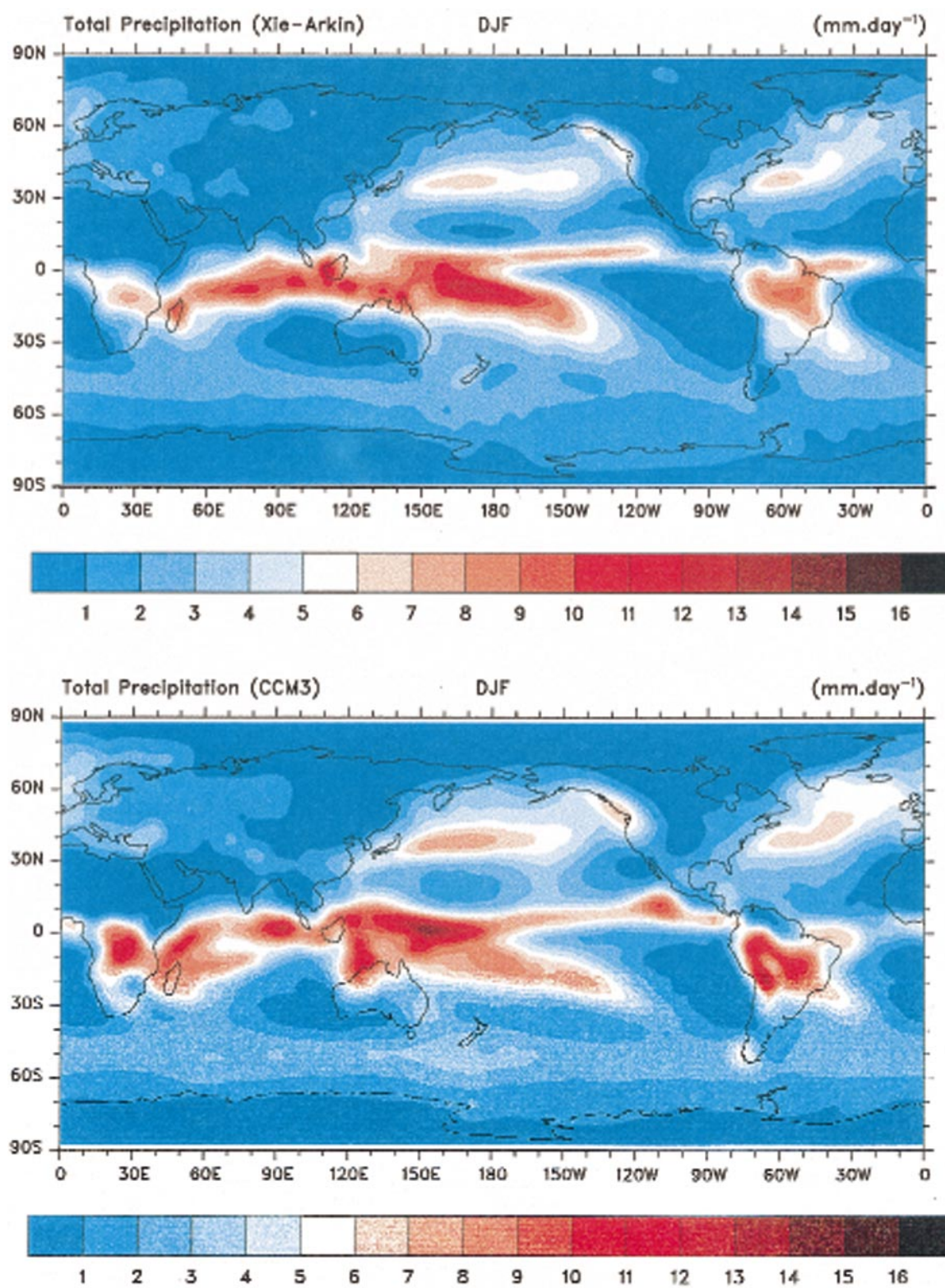
FIG. 21. Global DJF distribution of precipitation for the Xie and Arkin (1996) precipitation climatology, and as simulated by the CCM3.
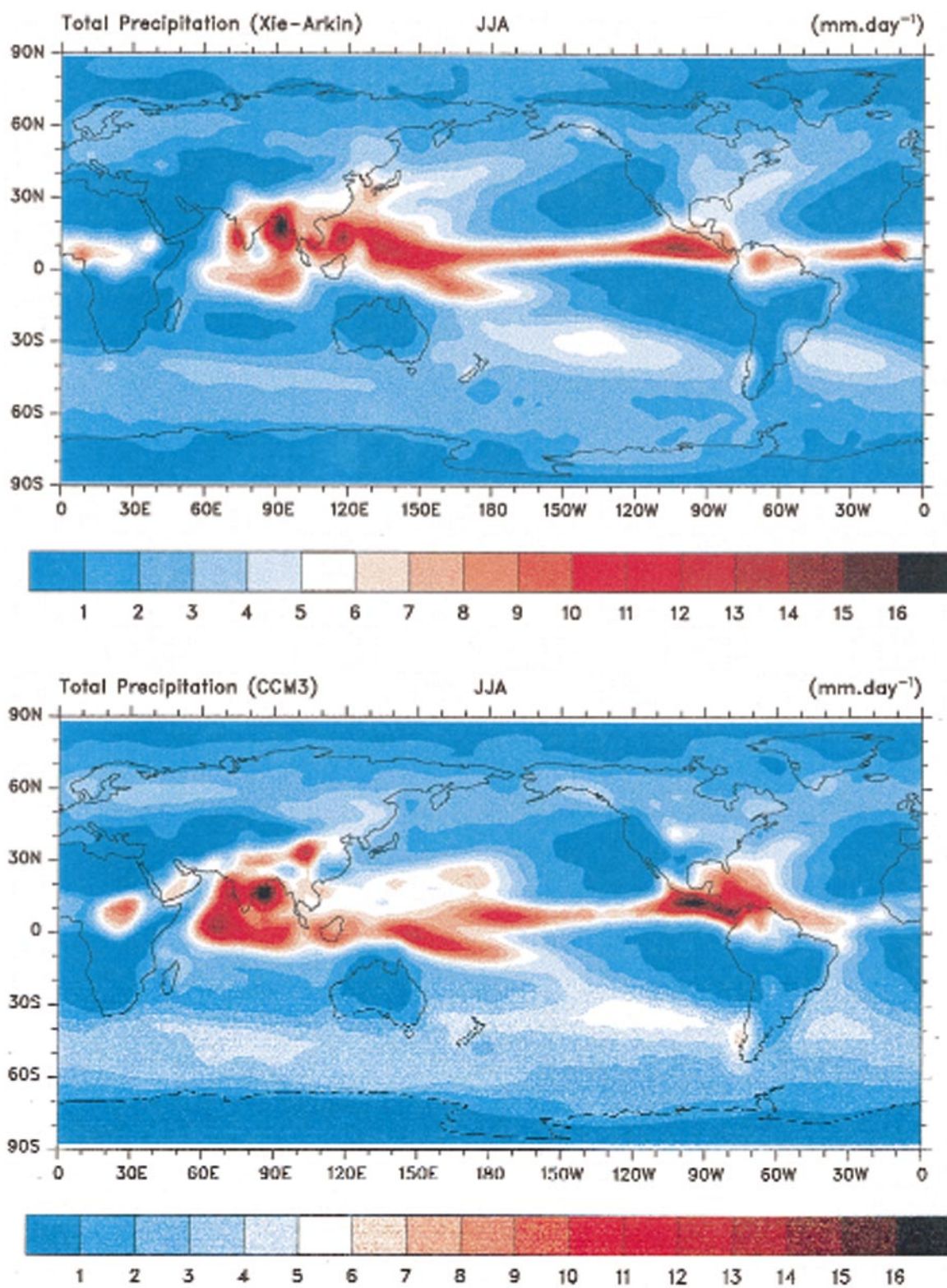
FIG. 22. Global JJA distribution of precipitation for the Xie and Arkin (1996) precipitation climatology, and as simulated by the CCM3.
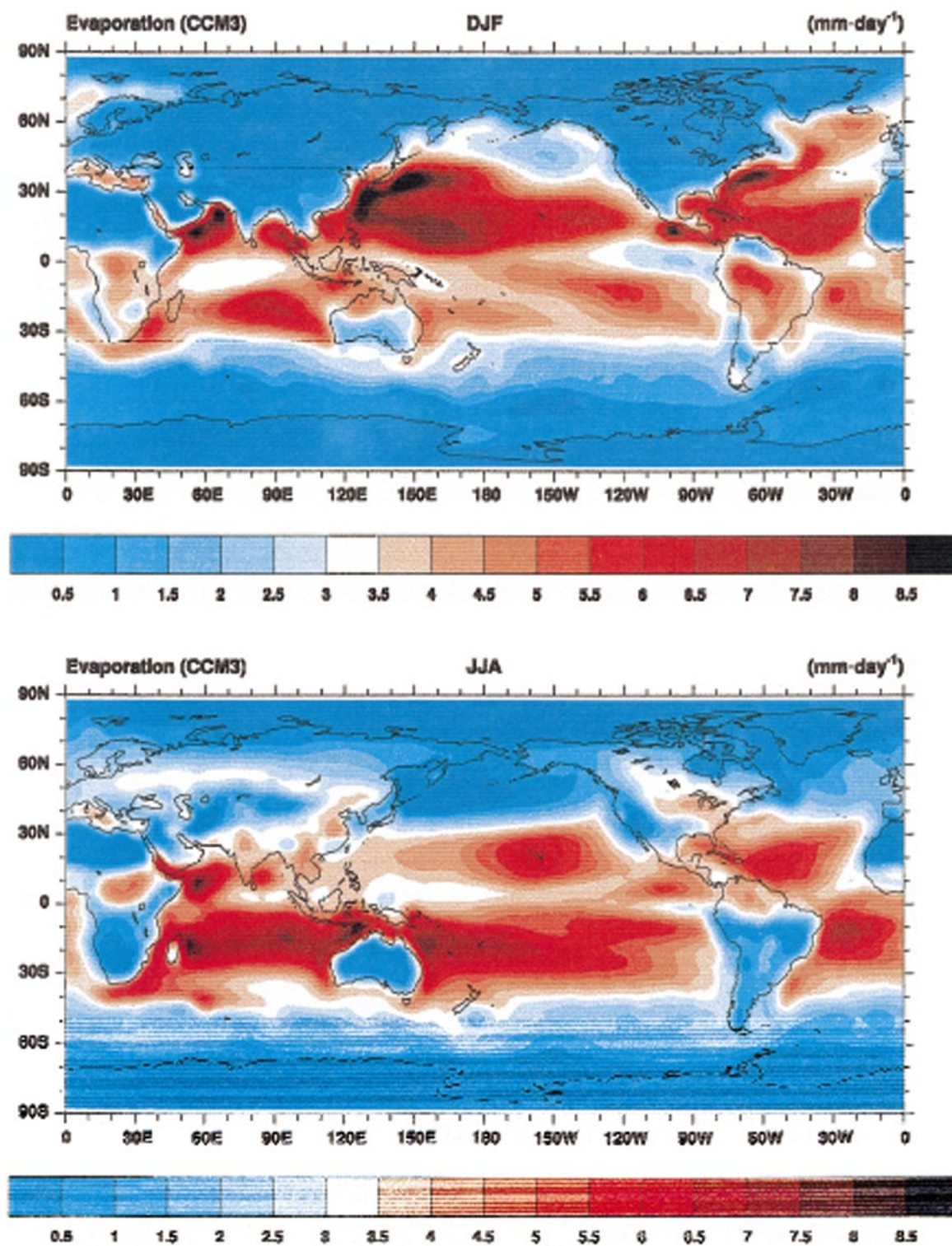
FIG. 23. Global seasonal distribution of evaporation as simulated by the CCM3 for DJF (top panel) and JJA (bottom panel).
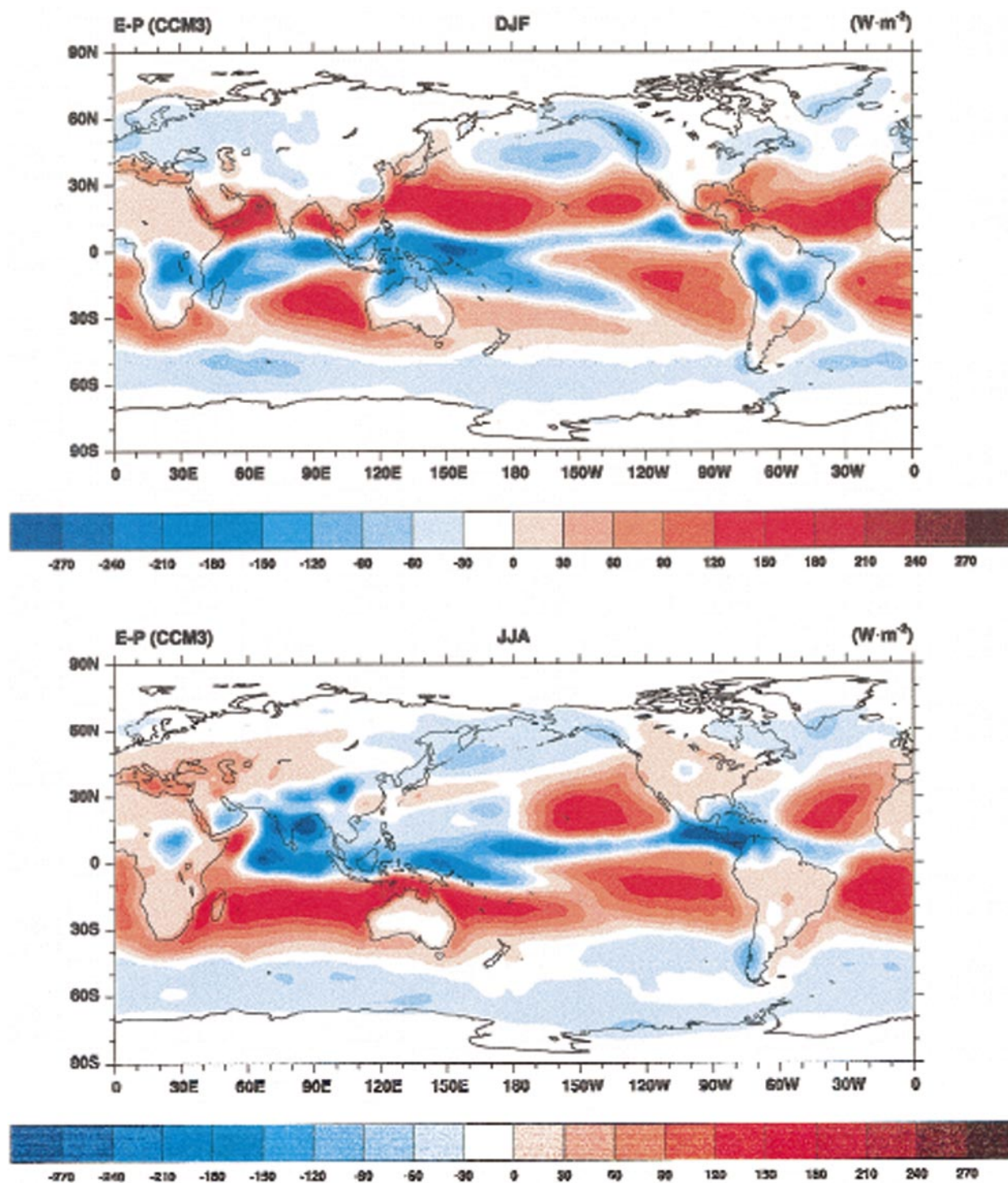
FIG. 24. Global seasonal distribution of $E - P$ as simulated by the CCM3 for DJF (top panel) and JJA (bottom panel).

mean. The subtropics are the clear source of water for the simulated general circulation, particularly in the Southern Hemisphere as suggested by the zonal mean shown in Fig. 17. A large seasonal cycle in $E - P$ exists over much of South America, central and southern Af-

rica, India, and southeast Asia, mostly a consequence of the seasonal migration of deep convection in response to solar insolation. Similar seasonal variability is seen over most of Europe extending into central Asia, and over North America. Most of Europe and a large portion
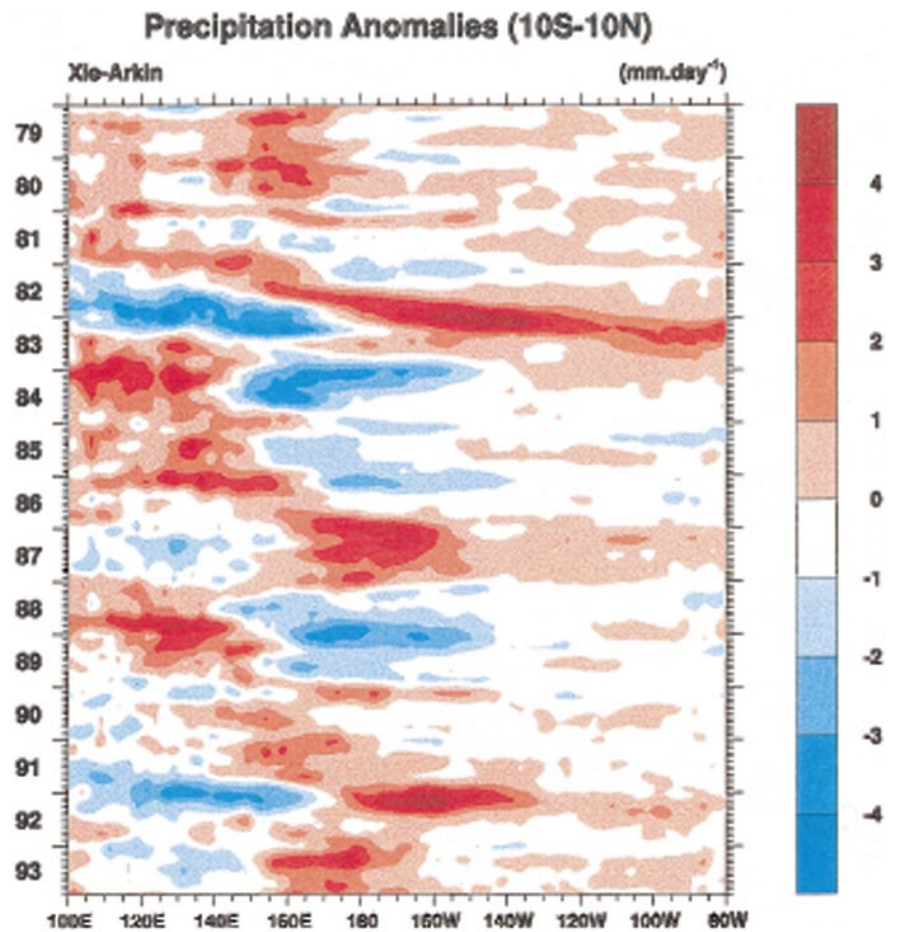
FIG. 25. Equatorial (10°N–10°S) precipitation anomalies for the 15-yr period 1979–93 as derived
from the Xie and Arkin (1996) precipitation climatology.

of North America can be characterized as water source regions during JJA, and water sink regions during DJF.

4. Simulated ENSO response

Equatorial SST anomalies associated with ENSO provide a very useful framework for evaluating observed local and extratropical responses in numerical simulations of climate. Here, we examine the sensitivity of the CCM3 simulation for the 1979–93 period, which includes a number of ENSO cycles, including the very strong 1982 ENSO event. ERBE provides a unique observational dataset on cloud radiative forcing for a portion of this period, which can be used to evaluate the simulated TOA response to ENSO forcing (e.g., Kiehl et al. 1998b). The Xie and Arkin (1996) dataset also provides a unique observational check on the simulated precipitation response to ENSO. Figures 25 and 26 are Hovmöller diagrams showing precipitation anomalies as estimated by Xie and Arkin over the equatorial region (averaged between 10°N and 10°S) for the period January 1979–December 1993, and for the CCM3 simulation for the period January 1979–July 1993. The Xie

and Arkin dataset shows strong positive precipitation anomalies in response to the major warming events extending eastward across the tropical Pacific. Similarly, a number of strong negative anomalies, corresponding to the cold phase of the observed ENSO cycle, are seen in the central Pacific. During the 1982 warm event, a large precipitation anomaly, exceeding 3 mm day^{-1}, clearly extends across the entire Pacific basin. The CCM3 does an exceptionally good job of capturing both the structure and magnitude of the anomaly pattern. The west-central Pacific anomalies are also generally well represented in the CCM3 simulation, where the eastward extension of the precipitation changes are very accurately reproduced, even for the weaker SST events.

The simulated ENSO response can also be illustrated by examining the longer-term average precipitation differences between a warm and cold event, an analysis techinque that helps to maximize the observed response. Figure 27 shows the seasonal differences between DJF 1987 and DJF 1989 (i.e., warm minus cold event) for the Xie and Arkin precipitation data and the CCM3. The Xie and Arkin dataset shows a very large increase in precipitation over the central Pacific, along
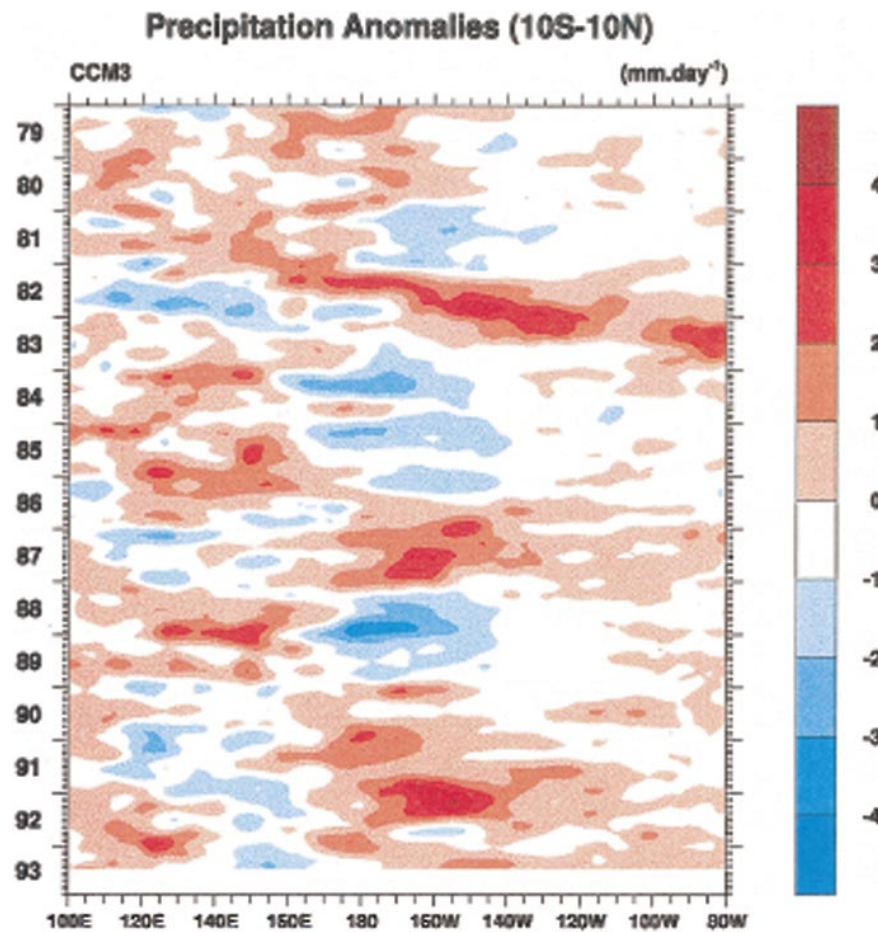
FIG. 26. Equatorial (10°N–10°S) precipitation anomalies for the 15-yr period 1979–93 as simulated by the CCM3.

with reductions to the west and south (e.g., in the SPCZ) of this region for the DJF seasonal average. The CCM3 does a very good job in reproducing this precipitation anomaly pattern. Although the positive anomaly does not exhibit the identical meridional extent, the general structure and magnitude of the response is very well captured. The nonlocal extratropical ENSO response pattern is considerably weaker, but is reproduced to a large extent over large portions of the Northern Hemisphere. In particular, note the positive precipitation anomaly over the southeastern United States and along the west coast of North America. Similar response patterns are seen over portions of the Eastern Hemisphere. During JJA (not shown) the Xie and Arkin data exhibits a positive anomaly centered in the western Pacific extending eastward across the entire Pacific basin, with weak negative anomalies flanking the maximum in the precipitation response. In this case, the CCM3 simulation of the ENSO response is not as good, where the maximum response is mislocated in the central Pacific with an anomalously large negative anomaly to the southwest. Despite the poor positioning, the equatorial response is reasonably well captured in the simulation

with a magnitude similar to what is indicated by the observational data. These results, as with most of the simulation properties that have been presented, represent a significant improvement in the CCM's precipitation sensitivity to variability in surface forcing.

5. Concluding remarks

We have illustrated selected aspects of the simulated thermodynamic structure and hydrologic cycle for the NCAR CCM3 in the context of parameterization changes to key thermodynamic and hydrologic components. The revised parameterizations have had a major impact on the simulated climate of the CCM, where many of the traditional measures of simulation quality are now much closer to observational estimates. Changes to the diagnosis of cloud optical properties and the incorporation of a sophisticated land surface model have greatly improved the surface energy budget and the corresponding simulation of the surface climate over land. This results in a considerably weaker annual cycle in hydrologic processes over land surfaces, which strongly influences the global behavior of the hydrologic
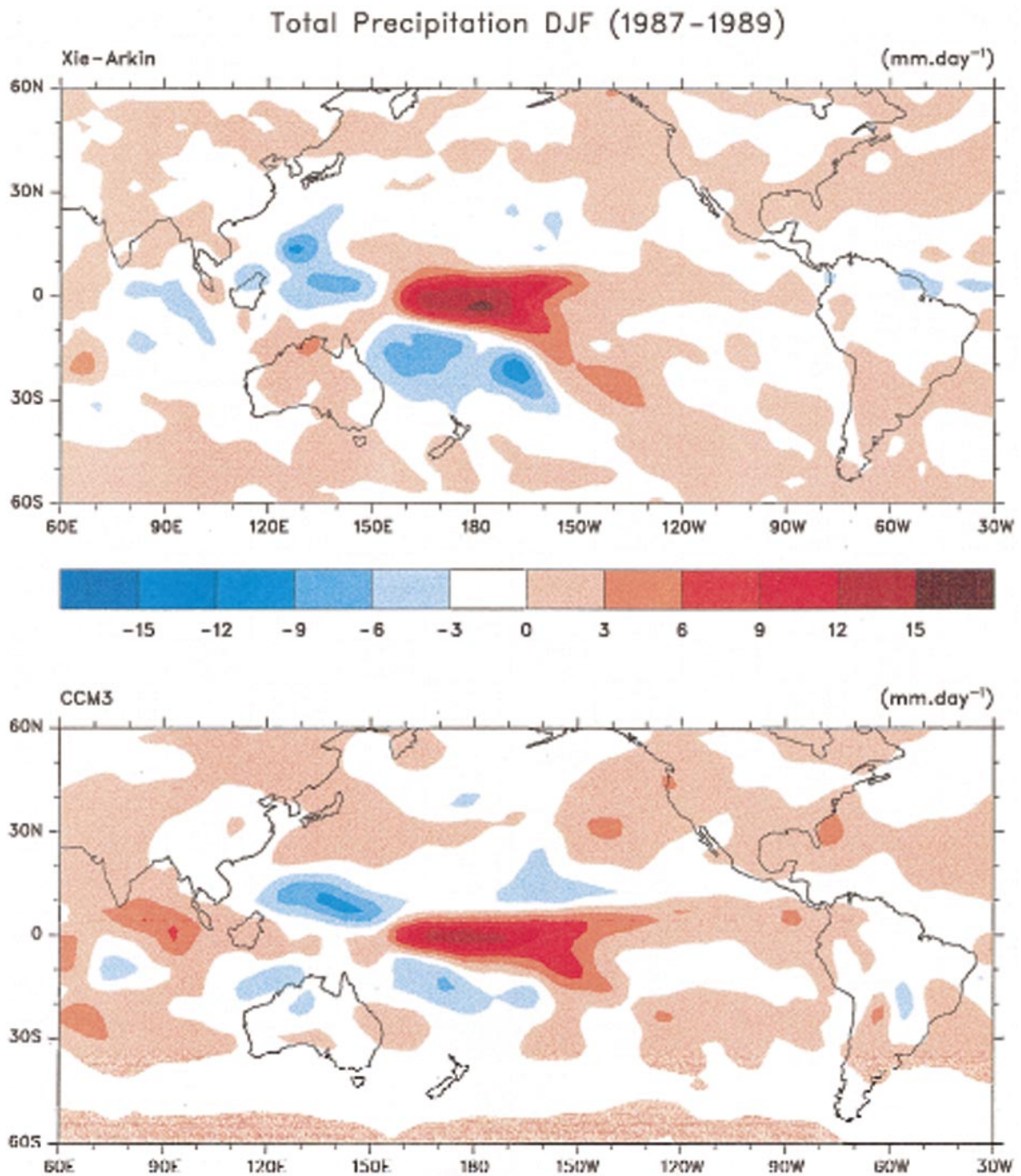
FIG. 27. DJF87–DJF89 (warm–cold) precipitation anomalies for the Xie and Arkin (1996) precipitation climatology (top panel) and CCM3 (bottom panel).

cycle. Modifications to the parameterization of the atmospheric boundary layer and moist convection also significantly alter, and generally improve, the simulated evaporation and precipitation characteristics, both globally and regionally.

The simulated temperature field in the Tropics is warmer in the CCM3 when compared to the CCM2, exhibiting a weak warm bias in the middle troposphere when compared to global analyses. This warming is in large part a response to the introduction of the Zhang and McFarlane (1995) scheme for deep convection, as is the more pronounced cold bias near the tropical tropopause. In most other respects the temperature field is not significantly changed when compared to the CCM2.

The zonally averaged large-scale moisture field provides a reasonable, albeit dry, representation of the analyzed zonal-mean structure. However, an examination of the global distribution of water vapor suggests the presence of large local errors in the simulation.

Simulated cloud water path shows pronounced extratropical peaks associated with storm tracks, and a relatively flat and weak distribution at low latitudes. Low-latitude differences between the CCM3 and the Greenwald et al. (1995) and Weng and Grody (1996) satellite-derived climatologies are quite large, where the ITCZ is a very weakly represented feature in the CCM3. The global seasonal cycle of the CCM3 and Greenwald cloud water path data is completely out of phase, even though the CCM's annual cycle in cloud forcing is consistent with ERBE observational estimates. These differences warrant further study, particularly because of differences in existing satellite climatologies of cloud water, which are presumably related to details in the retrieval techniques.

Meridional distributions of precipitation and evaporation rates show systematic reductions when compared to the CCM2, generally in the direction of observational estimates. Annual and seasonal average evaporation rates exhibit substantial reductions over most of the globe, particularly in the vicinity of deep tropical convection. Annual mean precipitation reductions are more uniformly distributed with latitude, although CCM3 − CCM2 differences in the seasonal amplitude of ITCZ precipitation are extremely large, where the CCM3 is much more consistent with observational estimates. These changes in evaporation and precipitation result in significant changes in the distribution of the net water exchange with the surface and the corresponding meridional transport of water by the simulated general circulation.

The CCM3's precipitation response to ENSO forcing is highly realistic, both in structure and amplitude. Anomalies in the simulated precipitation field reproduce observed patterns over the tropical Pacific, where the phase and amplitude of the response is well captured. Seasonal differences in precipitation for warm and cold events are also very well simulated, where both the pattern and amplitude of the response agree with observational estimates.

Despite many improvements in the simulated climate, there are a number of deficiencies in need of understanding so that improvements can be made to the appropriate physical parameterization. The large-scale moisture field exhibits a widespread lower-tropospheric dry bias, which is manifested in significant local errors of precipitable water. This bias is related to the CCM3 changes in the parameterization of moist convection, and seriously affects the simulated moist static stability at the lower latitudes. There are also a number of important errors in the tropical precipitation distribution, which have implications for anomalous forcing of the local surface climate and stationary wave structure. We

are continuing to develop a detailed understanding of these simulation biases in the context of the collection of parameterization processes that contribute to the total diabatic forcing of the atmosphere. It is only with an integrated approach to the problem that the underlying causes for existing biases will be completely understood so that physically justifiable modifications to the model formulation can be incorporated.

REFERENCES

Boer, G. J., and Coauthors, 1992: Some results from an intercomparison of the climates simulated by 14 atmospheric general circulation models. *J. Geophys. Res.,* **97,** 12 771–12 786.

Bonan, G. B., 1996: A land surface model (LSM version 1.0) for ecological, hydrological, and atmospheric studies: Technical description and user's guide. NCAR Tech. Note NCAR/TN-417+STR, 150 pp. [Available from NCAR, Boulder, CO 80307.]

——, 1998: The land surface climatology of the NCAR Land Surface Model (LSM 1.0) coupled to the NCAR Community Climate Model (CCM3). *J. Climate,* **11,** 1307–1326.

Boville, B. A., and P. R. Gent, 1998: The NCAR Climate System Model, version one. *J. Climate,* **11,** 1115–1130.

Cess, R. D., and Coauthors, 1990: Intercomparison and interpretation of climate feedback processes in nineteen atmospheric general circulation models. *J. Geophys. Res.,* **95,** 16 601–16 615.

Chahine, M. T., 1992: The hydrologic cycle and its influence on climate. *Nature,* **359,** 373–380.

Doney, S. C., W. G. Large, and F. O. Bryan, 1997: Surface ocean fluxes and water mass transformation rates in the coupled NCAR Climate System Model. *J. Climate,* **11,** 1420–1441.

Greenwald, T. J., G. L. Stephens, S. A. Christopher, and T. H. Vonder Haar, 1995: Observations of the global characteristics and regional radiative effects of marine cloud liquid water. *J. Climate,* **8,** 2928–2946.

Hack, J. J., 1994: Parameterization of moist convection in the National Center for Atmospheric Research Community Climate Model (CCM2). *J. Geophys. Res.,* **99,** 5551–5568.

——, 1998a: Sensitivity of the simulated climate to a diagnostic formulation for cloud liquid water. *J. Climate,* in press.

——, 1998b: An analysis of the improvement in implied meridional ocean energy transport as simulated by the NCAR CCM3. *J. Climate,* **11,** 1237–1244.

——, B. A. Boville, B. P. Briegleb, J. T. Kiehl, P. J. Rasch, and D. L. Williamson, 1993: Description of the NCAR Community Climate Model (CCM2). NCAR Tech. Note NCAR/TN-382+STR, 108 pp. [NTIS PB93-221802/AS.]

——, ——, J. T. Kiehl, P. J. Rasch, and D. L. Williamson, 1994: Climate statistics from the NCAR Community Climate Model (CCM2). *J. Geophys. Res.,* **99,** 20 785–20 813.

Hurrell, J. W., and G. G. Campbell, 1992: Monthly mean global satellite data sets available in CCM history tape format. NCAR Tech. Note NCAR/TN-371+STR, 94 pp. [Available from NCAR, Boulder, CO 80307.]

——, J. J. Hack, and D. P. Baumhefner, 1993: Comparison of NCAR Community Model climates. NCAR Tech. Note NCAR/TN-395+STR, 335 pp. [Available from NCAR, Boulder, CO 80307.]

——, ——, B. A. Boville, D. L. Williamson, and J. T. Kiehl, 1998: The dynamical simulation of the NCAR Community Climate Model: CCM3. *J. Climate,* **11,** 1207–1236.

Kalnay, E., and Coauthors, 1996: The NCEP/NCAR 40-year reanalysis project. *Bull. Amer. Meteor. Soc.,* **77,** 437–471.

Kiehl, J. T., 1994a: Sensitivity of a GCM climate simulation to differences in continental versus maritime cloud drop size. *J. Geophys. Res.,* **99,** 23 107–23 115.

——, 1994b: Clouds and their effect on the climate system. *Phys. Today,* **47,** 36–42.

——, 1998: Simulation of the tropical Pacific warm pool with the NCAR Climate System Model. *J. Climate,* **11,** 1342–1355.

——, and K. E. Trenberth, 1997: Earth's annual global mean energy budget. *Bull. Amer. Meteor. Soc.,* **78,** 197–208.

——, J. J. Hack, and B. P. Briegleb, 1994: The simulated earth radiation budget of the NCAR CCM2 and comparisons with the Earth Radiation Budget Experiment (ERBE). *J. Geophys. Res.,* **99,** 20 815–20 827.

——, G. B. Bonan, B. A. Boville, B. P. Briegleb, D. L. Williamson, and P. J. Rasch, 1996: Description of the NCAR Community Climate Model (CCM3). NCAR Tech. Note NCAR/TN420+STR, 152 pp. [Available from NCAR, Boulder, CO 80307.]

——, ——, ——, ——, D. L. Williamson, and P. J. Rasch, 1998a: The National Center for Atmospheric Research Community Climate Model: CCM3. *J. Climate,* **11,** 1131–1149.

——, ——, and J. W. Hurrell, 1998b: The energy budget of the NCAR Community Climate Model: CCM3. *J. Climate,* **11,** 1151–1178.

Lau, W. K.-M., Y. C. Sud, and J. H. Kim, 1995: Intercomparison of hydrologic processes in global climate models. NASA Tech. Memo. 104617, Goddard Space Flight Center, 161 pp. [Available from NASA GSFC, Greenbelt, MD 20771.]

Oberhuber, J. M., 1988: An atlas based on the ''COADS'' dataset: The budgets of heat, bouyancy and turbulent kinetic energy at the surface of the global ocean. Max-Planck Institute for Meteorology Rep. 15, 199 pp. [Available from Max-Planck-Institut für Meteorologie, Bundesstr. 55, D-20146 Hamburg, Germany.]

Randel, D. L., T. H. Vonder Haar, M. A. Ringerud, G. L. Stephens, T. J. Greenwald, and C. L. Combs, 1996: A new global water vapor dataset. *Bull. Amer. Meteor. Soc.,* **77,** 1233–1246.

Riehl, H., 1965: *Introduction to the Atmosphere.* McGraw Hill, 410 pp.

Rossow, W. B., and Y.-C. Zhang, 1995: Calculation of surface and top of atmosphere radiative fluxes from physical quantities based on ISCCP data sets. Part II: Validation and first results. *J. Geophys. Res.,* **100,** 1167–1197.

Stephens, G. L., and P. J. Webster, 1981: Clouds and climate: Sensitivity of simple systems. *J. Atmos. Sci.,* **38,** 235–247.

Sundqvist, H., 1988: Parameterization of condensation and associated clouds in models for weather prediction and general circulation simulation. *Physically-Based Modelling and Simulation of Climate and Climatic Change,* M. E. Schlesinger, Ed., Vol. 1, Kluwer Academic, 433–461.

Trenberth, K. E., and C. J. Guillemot, 1995: Evaluation of the global atmospheric moisture budget as seen from analyses. *J. Climate,* **8,** 2255–2272.

Warren, S. G., C. J. Hahn, J. London, R. M. Chervin, and R. L. Jenne, 1988: Global distribution of total cloud cover and cloud type amounts over the ocean. NCAR Tech. Note NCAR/TN-317+STR, National Center for Atmospheric Research, Boulder, CO. [Available from National Center for Atmospheric Research, P.O. Box 3000, Boulder, CO 80307-3000.]

Weng, F., and N. C. Grody, 1996: Retrieval of cloud liquid water using the Special Sensor Microwave Imager (SSM/I). *J. Geophys. Res.,* **99,** 25 535–25 551.

Wielicki, B. A., R. D. Cess, M. D. King, D. A. Randall, and E. F. Harrison, 1995: Mission to planet earth: Role of clouds and radiation in climate. *Bull. Amer. Meteor. Soc.,* **76,** 2125–2153.

Williamson, D. L., and J. G. Olson, 1998: A comparison of semi-Lagrangian and Eulerian polar climate simulations. *Mon. Wea. Rev.,* **126,** 991–1000.

Xie, P., and P. A. Arkin, 1996: Analyses of global monthly precipitation using gauge observations, satellite estimates, and numerical model predictions. *J. Climate,* **9,** 840–858.

Zhang, G. J., and N. A. McFarlane, 1995: Sensitivity of climate simulations to the parameterization of cumulus convection in the Canadian Climate Centre general circulation model. *Atmos.–Ocean,* **33,** 407–446.